CrvA and CrvB form a curvature-inducing module sufficient to induce cell shape complexity in Gram-negative bacteria

Nicholas R. Martin[1], **Edith Blackman**[1], **Benjamin P. Bratton**[1,2], **Katelyn J. Chase**[2], **Thomas M. Bartlett**[1,†], **Zemer Gitai**[1,*]

[1]Department of Molecular Biology, Princeton University, Princeton, NJ 08544, USA

[2]Lewis-Sigler Institute for Integrative Genomics, Princeton University, Princeton, NJ 08544, USA

Abstract

Bacterial species have diverse cell shapes that enable motility, colonization, and virulence. The cell wall defines bacterial shape and is primarily built by two cytoskeleton-guided synthesis machines, the elongasome and the divisome. However, the mechanisms producing complex shapes, like the curved-rod shape of *Vibrio cholerae,* are incompletely defined. Previous studies have reported that species-specific regulation of cytoskeleton-guided machines enables formation of complex bacterial shapes such as cell curvature and cellular appendages. In contrast, we report that CrvA and CrvB are sufficient to induce complex cell shape autonomously of the cytoskeleton in *V. cholerae*. The autonomy of the CrvAB module also enables it to induce curvature in the Gram-negative species *Escherichia coli, Pseudomonas aeruginosa, Caulobacter crescentus*, and *Agrobacterium tumefaciens*. Using inducible gene expression, quantitative microscopy, and biochemistry we show that CrvA and CrvB circumvent the need for patterning via cytoskeletal elements by regulating each other to form an asymmetrically-localized, periplasmic structure that directly binds to the cell wall. The assembly and disassembly of this periplasmic structure enables dynamic changes in cell shape. Bioinformatics indicate that CrvA and CrvB may have diverged from a single ancestral hybrid protein. Using fusion experiments in *V. cholerae,* we find that a synthetic CrvA/B hybrid protein is sufficient to induce curvature on its own, but that expression of two distinct proteins, CrvA and CrvB, promotes more rapid curvature induction. We conclude that morphological complexity can arise independently of cell shape specification by the core cytoskeleton-guided synthesis machines.

Cells come in a variety of shapes that contribute to fitness in diverse environments [1–4]. Bacterial species produce cellular geometries ranging in complexity from simple rods and spheres to corkscrews and star shapes [1,5,6]. These shapes are defined by a rigid cell wall made from peptide-crosslinked polysaccharide strands, termed peptidoglycan (PG)

*Correspondence to: zgitai@princeton.edu.
†Present address: Department of Microbiology, Harvard Medical School, Boston, MA 02115

[7]. Because this exoskeleton prevents lysis from the turgor pressure of the cytoplasm, construction of new cell wall must be highly regulated to maintain integrity during growth and division.

To spatially regulate cell wall growth, PG synthesis enzymes are coupled to asymmetrically-localized cytoskeletal elements through multiprotein transmembrane complexes. During cell division, the bacterial tubulin homolog, FtsZ, localizes to the mid-cell and directs the activity of its associated PG synthases to initiate septation [8,9]. Similarly, the actin homolog, MreB, directs a different set of PG synthases at the lateral surface of rod-shaped cells, thereby elongating the cylindrical surface to maintain rod shape [10,11]. These two molecular machines termed the divisome and the elongasome, respectively, constitute the "core" cell shape machinery responsible for determining the simple bacterial shapes of rods and spheres.

Evolution has elaborated on these basic forms to produce more complex shapes such as the curved-rod, which promotes motility and niche colonization in various species [1,6,12–14]. Studies in the curved-rod bacterium *Caulobacter crescentus* suggest that co-option of the MreB cytoskeleton led to the evolution of its complex cell shape. Specifically, the intermediate filament-like protein, CreS requires MreB to induce cell curvature in *C. crescentus* and can only curve bacterial species that possess MreB [15–17]. Similarly, MreB is required for the specialized PG synthesis complex that produces a cellular appendage called a stalk [18,19]. This adaptation of integral cytoskeletal machinery is a prevalent mechanism for generating morphological diversity across the domains of life, as eukaryotic systems also co-opt common cytoskeletal elements to generate species-specific or cell-specific structures [3,20,21].

The human pathogen *Vibrio cholerae* has a curved-rod shape that we previously showed requires the periplasmic filament-forming determinant, CrvA [13]. CrvA appears to have evolved independently from crescentin as they lack sequence homology and are localized to different cellular compartments [13]. Consequently, we sought to characterize the mechanism, dynamics, and evolution of *V. cholerae* curvature to both better understand the biology of this important human pathogen and to determine if co-opting core cell machineries is a universal mechanism by which bacteria form complex shapes.

Results

Two genes, *crvA* and *crvB,* are sufficient to induce cell shape complexity

To understand the origin of the complex cell shape of *V. cholerae* we sought to identify the complete set of factors required for its curved-rod morphology. The sequence downstream of the *crvA* gene encodes a larger gene with homology to *crvA,* which we named *crvB* (Extended Data Figures 1A and S1B). Like *crvA, crvB* is also required for curvature, as a *crvB* mutant is straight and (Figure 1A) complementation tests showed that *crvB* complemented *crvB,* but *crvA* and *crvB* could not cross-complement (Extended Data Figures 1C-S1E). Among the genomes of other *Vibrio* species, CrvA and CrvB homologs almost always occur together (Figure 1B). A singular exception, *Vibrio proteolyticus,* contains only a CrvA homolog and is reported to be a straight rod [22]. Furthermore, many

Vibrio species have neither a CrvA nor a CrvB homolog (Figure 1B) and are reported to be straight [22]. Thus, not only are CrvA and CrvB both required for cell curvature in *V. cholerae*, but their evolutionary co-occurrence correlates with cell curvature throughout the *Vibrio* genus.

To determine whether CrvA and CrvB are sufficient to induce curvature, we introduced them into the straight-rod species *Escherichia coli* and *Pseudomonas aeruginosa,* which both lack *crvA/B* homologs. In both cases, populations expressing a plasmid-borne operon of *crvA* and *crvB* had statistically-significant increases in median centerline curvature over those containing an empty vector (Figures 1C and Extended Data Fig. 2). Cells near the top of their respective curvature distributions (95th percentile) displayed a particularly pronounced difference in cell curvature (Extended Data Figure 2). This skew of the distribution toward high curvatures may indicate that only a subset of cells expressed the *crvAB* plasmid strongly enough to induce curvature (Figures 1C and Extended Data Fig. 2). Thus, *crvA* and *crvB* represent the complete set of *V. cholerae*-specific genes required for curvature, and function to induce cell shape complexity in heterologous, straight-rod species.

We next sought to determine if CrvA and CrvB are sufficient to induce curvature in a species that is not normally a straight rod. *C. crescentus* lacks *crvA/crvB* homologs but requires crescentin (*creS*) for curvature such that a *creS* mutant is a straight rod. Nevertheless, heterologous CrvA and CrvB expression significantly enhanced cell curvature in both wild-type *C. crescentus* and *creS* (Figures 1C and Extended Data Fig. 2). We note that this effect is modest, but statistically-significant, perhaps due to the use of a lower copy number plasmid. Thus, CrvA and CrvB are sufficient to induce curvature in another curved-rod bacterium but through a mechanism orthogonal to the native mechanism of curvature generation.

CrvA and CrvB form a module that functions autonomously of core shape machineries

Having identified the factors necessary for curvature in *V. cholerae* and sufficient to induce curvature in species that contain MreB and FtsZ, we set out to determine if they function like crescentin by co-opting the bacterial cytoskeleton. Previously, we found that curvature is robust to inhibition of the divisome, suggesting its activity is not required for curvature induction in *V. cholerae* [13]. To determine whether the elongasome is required for CrvAB function, we took advantage of the phylogenetic diversity of rod-shaped bacteria. *V. cholerae, E. coli, P. aeruginosa,* and *C. crescentus* use the MreB-directed elongasome to insert new PG throughout the lateral surface of the cell [10,18,23,24], but some bacteria form rods via a distinct growth pattern. The α-proteobacterium *Agrobacterium tumefaciens* lacks many canonical elongasome members including MreB, and instead propagates as a rod through a combination of FtsZ-patterned growth at the midcell, and FtsZ-independent growth from the cell pole [25,26]. Consistent with its MreB-dependence, crescentin cannot curve *A. tumefaciens* [16]. In contrast, CrvA and CrvB expression induced curvature in *A. tumefaciens* (Figures 1C and Extended Data Fig. 2). Thus, CrvAB act as a modular unit sufficient to induce curvature in heterologous species both straight and curved, as well as those that use either MreB-driven lateral growth or FtsZ-mediated polar growth.

Thus far we have demonstrated CrvAB function without FtsZ activity in *V. cholerae*, and without MreB in *A. tumefaciens.* To further test the dependence of the CrvAB module on the core shape machineries within a single biological context, we inhibited the MreB-associated elongasome and the FtsZ-associated divisome in *E. coli* expressing CrvAB. Treatment with A22 induced a dose-dependent widening of cells (Figures 2A and S3A) indicating that the A22 treatment was disrupting MreB [27]. Even in the absence of A22, CrvAB expression does not lead to significant curvature induction at the pre-treatment time point, but at all A22 concentrations tested, CrvAB expression led to a significant increase in cell curvature by the end point of the experiment (Figures 2A-B). We also treated wild-type *V. cholerae* with A22 and obtained similar results (Extended Data Figures 3B-D). Furthermore, in *E. coli,* CrvAB expression induced curvature during simultaneous treatment with A22 and the divisome inhibitor, cephalexin (Figure 2C). Therefore, the activity of the CrvAB module is robust to the simultaneous inhibition of both cytoskeleton-guided growth machines.

Though they are not known to be spatially-regulated, other PG enzymes function outside of the elongasome and divisome complexes. These most prominently include the bifunctional penicillin binding proteins PBP1A and PBP1B[28]. We deleted each of these genes in *V. cholerae* and found that neither was required for curved morphology (Extended Data Figure 3E). While there remain multiple other redundant PG enzymes that could potentially interact with CrvAB, these findings support the conclusion that the CrvAB module is functionally independent from the asymmetrically-localized core shape machines.

CrvA and CrvB break symmetry by assembling a periskeletal filament

How can CrvA and CrvB impact the shape of the cell wall independently of the core shape machines? Patterning cell growth requires both the ability to break symmetry and transmit that asymmetry to the cell wall. We tagged CrvA and CrvB with mCherry and msfGFP, respectively and found that each fusion protein (CrvA-mCherry and CrvB-GFP) was functional (Extended Data Figure 4A) and localized as a filamentous structure at the inner curved surface of the cell that persisted as cells grew (Figures 3A, S4B, and Supplementary Video 1). Furthermore, CrvA-mCherry and CrvB-GFP formed this asymmetrically-localized filament in *E. coli* (Figures 3A and S4C). When growing cells were observed by time-lapse microscopy, CrvAB filaments formed at straight segments and preceded the formation of curvature at that site. When elongated with cephalexin, cells often bend due to physical confinement, but we did not observe CrvAB filaments re-localize to the resulting CrvAB-independent cell curvatures (Supplementary Videos 2-3). Thus, we hypothesize that CrvAB does not actively sense cell curvature like MreB does[10,29,30], but rather that CrvAB produces curvature wherever it localizes.

Both CrvA and CrvB have N-terminal secretion signals and we previously observed CrvA-GFP in outer membrane vesicles (OMVs), which are typically periplasmic in origin [13]. To determine whether CrvB is periplasmic, we labelled the periplasm by fusing mCherry to the secretion signal of the periplasmic protein DsbA [31]. Sublethal inhibition of transglycosylase activity with moenomycin causes cells to round up and the periplasm visibly protrudes from the cytoplasm [32]. This allowed us to visualize full-length CrvA-GFP filaments in mCherry-

labelled regions that were unambiguously periplasmic (Figure 3B). CrvB-GFP filaments colocalized with DsbA-mCherry, indicating that CrvB is also periplasmic (Figure 3B). CrvA-mCherry and CrvB-GFP filaments remained colocalized in rounded moenomycin-treated cells, indicating that their colocalization to this periskeletal structure does not depend on the wild-type cellular geometry (Figure 3B).

CrvA directly binds the PG cell wall

How is the asymmetric localization of the CrvAB module converted into a corresponding asymmetry in cell shape? We first determined whether CrvAB are direct load-bearing shape determinants by exploiting our previous observation that CrvA filaments rapidly disassemble in hyperosmotic media [13]. Upon shift to hyperosmotic media, both CrvA-GFP and CrvB-GFP structures rapidly became diffuse, but morphology remained unchanged in these cells lacking CrvA or CrvB filaments, indicating that cellular geometry is not mechanically dependent on CrvAB filaments (Extended Data Figure 4D).

Previously, we measured a *crvA*-dependent reduction in PG insertion at the inner curved surface of the cell (where CrvAB filaments localize) relative to the outer face of the cell in *V. cholerae*[13]. Because the PG is chemically similar among bacteria[33], a direct interaction between periplasmic CrvAB filaments and the cell wall could explain the unprecedented range of species in which CrvAB are functional. To test this hypothesis, we purified CrvA and measured its ability to co-sediment with purified cell walls upon centrifugation at relatively low speeds that do not pellet proteins or protein polymers. As controls, we confirmed that purified WGA, a well-characterized PG-binding protein, but not purified GFP, associated with cell walls in this assay (Figure 3C). Similar to WGA, CrvA robustly co-sedimented with PG (Figure 3D). We confirmed that CrvA was only detected in the pellet fraction when PG was present, indicating that CrvA does not sediment independently and suggesting that CrvA directly binds to the PG cell wall (Figure 3D).

The evolution of the CrvAB cell shape module

Why does the CrvAB module require two proteins? CrvA and CrvB are homologs, but neither protein cross-complements suggesting that they are specialized. The most striking difference in their amino acid sequences is a ~250 residue C-terminal domain of CrvB that is not present in CrvA (Extended Data Figure 1B). Deletion of either this CrvB-specific (CBS) domain or the N-terminal domain (NTD) of CrvB abolished curvature (Figures 4A and 4B). Thus, the CBS domain is necessary, but not sufficient for CrvB function. Surprisingly, when we fused the CBS domain to the C-terminus of CrvA, the resulting chimeric protein, CrvA$_{CBS}$, induced curvature in a *crvAB* background (Figures 4A and 4B) and an msfGFP-tagged fusion (CrvA$_{CBS}$-GFP) forms filaments at the inner curve of the cell (Extended Data Figures 5A and 5B).

While *crvA$_{CBS}$* was sufficient to curve cells, these cells did not become as curved as wild type (Figure 4B) and curved more slowly (Figure 4C). In wild-type *V. cholerae,* cell curvature rapidly decreases when saturated cultures are diluted into fresh media and increases until the culture reaches stationary phase [13] (Figure 4C). Cells with *crvA$_{CBS}$* took nearly twice as long to return to maximum curvature (Figure 4C). We expressed a

second copy of $crvA_{CBS}$ at the $crvB$ locus (2xCrvA$_{CBS}$) and found that this mitigated the reduction in maximum curvature, but not the slower dynamics (Figures 4A-C). Therefore, a CrvA/CrvB hybrid functions as a minimal curvature-inducing factor but the two-gene CrvAB module found in WT *V. cholerae* induces curvature more rapidly.

The division of functional domains among CrvA and CrvB suggested the possibility that the CrvAB module evolved from an ancestral protein resembling CrvA$_{CBS}$. Phylogenetic analysis of CrvA/CrvB homologs revealed a set of sequences, which we refer to as CrvY, that resemble a CrvA$_{CBS}$ chimera in clades related to *Vibrios* such as *Aliivibrios* (Extended Data Figures 6A-C). CrvY has a CBS domain like CrvB but has an NTD more similar to the NTD of CrvA than CrvB (Figure 4D). Deletion of $crvY$ (*VF_A0834*) from the curved species *Aliivibrio fischeri* produced straight cells and heterologous expression of $crvY$ in *V. cholerae* was sufficient to induce curvature in a $crvAB$ mutant (Figures 4E-F and S6D-E). The necessity of CrvY for curvature in *A. fischeri* and sufficiency in *V. cholerae* indicate that CrvY is a functional, extant form of a CrvA$_{CBS}$ chimera. Thus, our data suggest that the CrvAB module evolved by the duplication and specialization of a single ancestral gene.

Specialization of CrvA and CrvB drives filament assembly and curvature dynamics

We next determined how the specialization of CrvA and CrvB relates to their filament assembly. Deleting $crvA$ resulted in diffuse CrvB-GFP localization, indicating that CrvA is required for CrvB assembly (Figure 5A). Deleting $crvB$ also disrupted CrvA-GFP, but in a qualitatively different manner. While most $crvB$ cells still exhibited well-defined CrvA-GFP structures, these cells typically exhibited multiple small CrvA-GFP puncta and only ~6% had long CrvA-GFP filaments like those seen in wild type (Figure 5A). We hypothesized that the function of CrvB was to potentiate the higher-order assembly of these smaller CrvA-GFP structures into larger filaments. To test this, we controlled $crvB$ transcription with arabinose-induction (P$_{bad}$) from an ectopic locus and observed the effect of $crvB$ expression on CrvA-GFP assembly. Consistent with our hypothesis, arabinose induction up to 0.005% increased CrvA-GFP assembly (Figures 5B and 5C) and cell curvature (Figures 5B and 5D) in a dose-dependent manner. Interestingly, $crvB$ induction beyond 0.005% caused curvature and CrvA-GFP assembly to trend downward and CrvA-GFP formed bright, polar foci (Figures 5B and 5D). This suggested that there may be an optimal CrvA:CrvB stoichiometry below which CrvB interferes with CrvA assembly, and curvature.

To measure the CrvA:CrvB stoichiometry, we repeated the $crvB$ induction and measured the levels of CrvA-GFP by western blot. We estimated the amount of CrvB present by including a strain wherein the arabinose-inducible $crvB$ allele is GFP-tagged rather than the natively controlled $crvA$ allele. We then quantified the CrvA-GFP and CrvB-GFP bands relative to the housekeeping gene RpoA. While CrvA-GFP levels were constant, CrvB-GFP levels spanned almost two orders of magnitude as a function of arabinose concentration and CrvA-GFP concentration always exceeded CrvB-GFP concentration (Figures 5E and Extended Figure 7a). Under optimal curvature-simulating conditions (0.005% arabinose) CrvA-GFP concentration was about 6-fold higher than CrvB-GFP concentration with that ratio decreasing to about 2-fold at 0.1% arabinose where median curvature is significantly

lower (Figures 5D-E and Extended Figure 7a). The favorability of a higher CrvA:CrvB stoichiometry is consistent with native conditions, as CrvA-GFP is more abundant than CrvB-GFP when they are each under their native promoters (Figure 5F). Thus, at the physiological CrvA concentration, CrvB promotes robust filament assembly and curvature, but at high CrvB:CrvA ratios both assembly and curvature are disrupted.

If CrvB is only required to promote the assembly of CrvA at the physiological CrvA concentration, then *crvA* overexpression may be sufficient for CrvB-independent curvature. To test this, we expressed CrvA-GFP in *E. coli* from a tetracycline-inducible (P_{tet}) plasmid. Without CrvB, CrvA-GFP overexpression with up to 1ng/mL anhydrotetracycline (tet) caused curvature to trend higher than the empty vector control, but it did not significantly increase median cell (Figures 6A and 6B). Similarly, CrvB-GFP overexpression alone had no effect on curvature (Extended Data Figures 7C-E). In contrast, even basal expression from the P_{tet} promoter induced curvature when we coexpressed CrvA-GFP with CrvB (Figures 6A and 6B). We confirmed by western blot that tet induction elevated CrvA-GFP concentration above levels present during coexpression (Extended Data Figure 7B). Therefore, CrvA overexpression may increase cell curvature, but coexpression of the full CrvAB module produces robust curvature.

Finally, we wondered how the combined functions of CrvA and CrvB come together to regulate cell shape in real time. First, we simultaneously observed CrvA-GFP assembly and cell curvature in a wild-type *V. cholerae* background where population curvature is dynamic. Cell curvature decreased as CrvA-GFP filaments were lost, and in these straight cells, CrvA-GFP formed multiple small structures resembling those in *crvB* (Figure 6C). In addition, cell curvature only began to increase after long CrvA-GFP filaments became prevalent (Figure 6C). These population-level dynamics were also observed in time-lapse movies of single cells. Upon dilution, curved stationary phase cells with CrvAB filaments exhibit a rapid drop in curvature as growth and division rapidly outpace new CrvAB filament formation (Supplementary Video 4). Later, CrvAB filaments form *de novo* in straight cells and mark the sites of future curvature as the cells gradually reestablish CrvAB assembly and curvature (Supplementary Video 4). Finally, we showed that manipulating the levels of CrvAB alter curvature dynamics, as overexpressing CrvAB increased cell curvature sooner than control cells (Extended Data Figure 8).

Discussion

CrvA and CrvB have specialized roles in generating cell curvature

In addition to the genetic evidence suggesting unique roles for CrvA and CrvB, our cell biological description of their roles in filament assembly provides a mechanistic basis for their asymmetry-generating activity. The function of CrvA to assemble small, CrvB-independent structures is likely due to assembly-promoting coiled-coil domains in the N-terminal region of the protein where CrvA shares greater homology with CrvY relative to CrvB[13]. Rather than forming CrvA-independent structures, CrvB promotes higher order CrvA assembly through its CBS domain that can even be functional when directly attached to CrvA, as in the CrvA$_{CBS}$ chimera that readily forms large filaments (Extended Data Figure 5A). However, our titration of CrvB levels suggests that for optimal curvature

induction, CrvA must be present in excess of CrvB (Figures 5B-D). The stoichiometry of the N-terminal and CBS domains is fixed at 1:1 in a CrvA/CrvB hybrid, suggesting that splitting these domains among two genes may have allowed the evolution of a more favorable stoichiometry of N-terminal domains to CBS domains. This may also explain why merely increasing the dosage of $CrvA_{CBS}$ was not sufficient to recover wild-type curvature dynamics, which could have significant functional implications for a rapidly-growing pathogen like *V. cholerae* (Figure 5C).

PG binding could enable CrvAB to regulate cell shape independently of the core shape machinery

While the enzymes bacteria use to build PG are numerous, functionally redundant, and may differ between species, the cell wall itself is largely similar in composition among Gram-negative bacteria[33]. It is impossible to rule out interaction with every cell wall enzyme, but we found that CrvAB can induce curvature independently of the MreB-dependent elongasome, the FtsZ-dependent divisome, PBP1a, and PBP1b, which include all known spatially-regulated PG synthesis complexes and the enzymes that produce the bulk of total PG. In contrast to previously-characterized shape determinants, the combination of periplasmic localization, filament formation, and direct PG binding suggest a unique mechanism wherein CrvAB filaments directly interact with the cell wall to locally slow its expansion. The compressive force from a PG-bound filament would locally resist the expansion of the cell wall by growth and may explain our previous finding that CrvA locally slows PG insertion[13]. Alternatively, CrvAB could locally inhibit the activity of an as-yet-unidentified cell wall synthesis enzyme.

Autonomous modules: a distinct class of cell-shape determinant

The surprising ability of the CrvAB module to function in heterologous species separated by 2.5 billion years of evolution [34] suggests a previously-undescribed route for the evolution of cell shape complexity. Previous studies of crescentin and SpmX identified MreB co-option as a strategy for producing complex shapes, but these mechanisms only function in species that possess MreB[17,35]. In contrast, we show that CrvAB can heterologously add new geometric features by both generating asymmetry and inhibiting cell wall growth through direct PG binding. As a result, the CrvAB module can even curve species that lack MreB such as *A. tumefaciens*. There are multiple complex bacterial morphologies for which no determinants have been identified. Our work suggests that these diverse forms may be built not by co-option of core cell biology, but by autonomous cell shape modules like the one that makes *V. cholerae* curved.

Materials and Methods

Bacterial strains and growth conditions

Bacterial strains and plasmids used are listed in Supplementary Table 1. *Vibrio cholerae*, *Escherichia coli*, *Pseudomonas aeruginosa* were cultured in LB medium (10g/L NaCl (Sigma), 10g/L tryptone (Bacto), 5g/L yeast extract (Bacto)) at 37°C with aeration. *Agrobacterium tumefaciens* was cultured in LB medium at 30°C with aeration. *Aliivibrio fischeri* was cultured either on LB agar (Bacto) plates or in LM liquid medium (20g/L

NaCl, 10g/L tryptone, 5g/L yeast extract) at 30°C with aeration. For *A. fischeri* curvature measurement, colonies from of wild-type or *crvY* from LB agar plates were suspended in LM and grown for 4h at 30°C. *Caulobacter crescentus* was grown in PYE medium (2g/L peptone (Bacto), 1g/L Yeast extract, 1mM $MgSO_4$ (Sigma), 0.5mM $CaCl_2$(Sigma)) at 30°C with aeration. Cultures in Figures 4C, 5B-E, and 6E were grown in 2mL culture volumes, while all other experiments were conducted in 5mL culture volumes unless otherwise indicated. Chromosomal mutations in *V. cholerae* and *A. fischeri* were made using suicide vectors pKAS32 [36] and pRE112 [37], respectively. Plasmids were introduced by conjugal transfer from *E. coli* S17 into *V. cholerae*, *C. crescentus*, *A. tumefaciens,* and *A. fischeri.* Plasmids were introduced by electroporation into *P. aeruginosa* and *E. coli MG1655.* Antibiotics were used in the following concentrations: Kanamycin 50μg/mL (*V. cholerae*, *E. coli*), Carbenicillin 25μg/mL (*A.* tumefaciens), Carbenicillin 200μg/mL (*P.aeruginosa*), Chloramphenicol 1μg/mL (*C.* crescentus).

Microscopy

Images were obtained using a Hamamatsu ORCA-Flash4.0 Digital CMOS camera on either a Nikon 90i microscope with a Nikon 100x Plan Apo NA=1.40 oil immersion objective lens or a Nikon Ti-E microscope with a Nikon 100x Plan Apo NA=1.45 oil immersion objective lens. For fluorescence, GFP-L and Cy5 HYQ filter cubes (90i) or GFP-HQ and mCherry filter cubes (Ti-E) were used to visualize msfGFP and mCherry fluorescent fusions, respectively. Excelitas X-Cite 120 LED*Boost* was used for illumination on both microscopes. All hardware was controlled by NIS Elements (version 4.60.00). Suspensions of *A. fischeri* cells were spotted on 1–2% (weight/volume) low melting point agarose (Invitrogen) pads of LM for imaging. For all other species, 1–2% low melting point agarose pads of M9 Salts (47.8mM Na_2HPO_4(Sigma), 22mM KH_2PO_4(Sigma), 8.6mM NaCl, 18.6mM NH_4Cl(Sigma)) were used. For growth on pads, LB liquid cultures of *V. cholerae* were spotted on 1–2% low melting point agarose pads of M9 supplemented with 2mM $MgSO_4$ (Sigma), 100μM CaCl2 (Sigma), and 0.5% glucose (Sigma) and incubated at 25°C throughout the experiment. All geometric measurements were performed on phase-contrast images at 100X magnification. For merged images, problems with filter alignment were manually corrected by adjusting contrast such that the cell body but not features within the cell were clearly visible. The image plane was then shifted so that outline of this fluorescence was aligned to the phase-contrast image or other fluorescent channel.

Measurement of cellular geometry

Phase images were analyzed using the MATLAB script Morphometrics [10] to segment cell contours and fit them with centerlines. Contours touching adjacent cells or having visible cleavage furrows were excluded from analysis to avoid overestimation of curvature due to the orientation of neighboring cells or recently divided cells. Curvature is root mean squared curvature of the centerline in units of inverse microns (μm^{-1}). Width is mean width of the contour along the entire centerline in microns (μm). Population measurements are from pooled measurements of cells from two or three biological replicates performed on different days. To account for differences in the number of cell contours in each replicate, an equal number of cells were randomly selected from each replicate before pooling. Violin plots represent one such randomized population. Populations that were also measured for

CrvA/CrvB-msfGFP filament assembly were not randomized because only the first 100 valid contours from each replicate were analyzed; therefore, all three replicates had an equal number of contours. For statistical tests of populations, the Wilcoxon two-sided rank sum test was used. For tests on randomized populations, the random sampling and statistical testing was repeated one thousand times and the mean p-value was reported to minimize the effect of any one sub-sample. p-values not reported on figures are in Supplementary Table 3. Representative cells shown in Figures 1A, 1C, 2A, 4A, 4E-F, and 6B, Extended data figures 1C-E, 2C, 3B, 3E, 4A, 4C, 5B, 6D-E, 7C, and 8A are representative of the 3rd quartile of length in their respective populations to facilitate visual comparison of cells with similar lengths. Unless otherwise indicated, these cells represent the 95th quantile of curvature in their respective populations.

Measurement of CrvA/CrvB-msfGFP filament assembly

Phase/GFP image stacks were split into their constituent channels and the phase channel was used to obtain cell contours using Morphometrics. After excluding touching and dividing cells as described above, the first 100 contours from each sample were superimposed on the corresponding GFP image. The GFP signal of each contour was manually inspected and categorized as "assembled" if most of the fluorescence signal formed a single, linear structure at least half the length of the cell. This was repeated on contours from three biological replicates performed on different days and pooled for population measurements (300 cells total). The Agresti-Coull method was used to estimate the 95% confidence intervals of this measurement and the center of this interval is reported as the proportion of the population that has assembled GFP structures. This proportion is referred to as the "assembly" of the population and is expressed as a percentage.

Complementation and heterologous expression of *crvA*, *crvB*, and *crvY*

For *crvA* or *crvB* expression, plasmid-borne alleles were placed under the control of a tetracycline-inducible promoter [38] and the following ribosome-binding site: AGGAGCTAAGGAAGCTAAA. When expressed together, both open reading frames are under control of the same promoter separated by the same ribosome-binding site. The same expression fragment was cloned into different plasmid backbones when required for heterologous expression. Anhydrotetracycline was added at the beginning of subculture in the following concentrations with a final culture volume of 5mL: 0ng/mL for *V. cholerae*, *E. coli*, and *P. aeruginosa*; 2ng/mL for *A. tumefaciens*; 5ng/mL for *C. crescentus*. For *V. cholerae*, *E. coli*, and *P. aeruginosa* saturated overnight cultures were diluted 1:1000 into LB with appropriate antibiotics and grown for 6h before imaging. For overexpression in *E. coli*, cultures were treated with indicated concentrations of anhydrotetracycline and cells were imaged at 5h instead of 6h. For *C. crescentus* saturated overnight cultures were diluted 1:100 into PYE with appropriate antibiotics and grown for 7h before imaging. For *A. tumefaciens* saturated overnight cultures were diluted 1:20 into LB with appropriate antibiotics and grown for 6h before imaging. For *crvY* expression in *V. cholerae* Δ*crvAB*, a plasmid-borne *crvY* allele from *A. fischeri* was placed under the control of an arabinose-inducible promoter [39] and the ribosome-binding site above. 0.1% L-Arabinose (Sigma) was added to LB with Kanamycin at the beginning of subculture with a final culture volume of 5mL. Saturated

overnight cultures were diluted to an optical density (OD_{600}) of 0.001 and grown for 4h before imaging.

Sublethal treatment with A22, Cephalexin, and Moenomycin

For moenomycin treatment, saturated overnight LB cultures were diluted 1:1000 into fresh LB supplemented with 500ng/mL moenomycin (Cayman #15506) and incubated at 37°C for 5–6h before imaging. Representative cells were chosen such that their orientation relative to the imaging plane allowed visual resolution of the periplasmic and cytoplasmic spaces. For A22 and cephalexin treatment in *E. coli*, saturated overnight LB cultures were diluted 1:1000 into fresh LB and grown for 4h after which pre-treatment samples were imaged. At 4h, 10μg/mL cephalexin or A22 at indicated concentrations were added. For A22 (gift from Doug Weibel and Randy Morgenstein) treatment cells were grown for an additional 4h before imaging. For Cephalexin (Sigma C-4895) treatment, and simultaneous A22+cephalexin treatment cells were imaged 2h after drug addition. A22 treatment in *V. cholerae* was performed as in *E. coli* except that A22 was added at 2h post dilution rather than 4h.

Titration of *crvB* expression in *V. cholerae*

crvB was deleted in a strain background expressing *crvA-msfGFP* from the native locus producing NM149. Into this background, a wild-type *crvB* was introduced at an ectopic locus on the opposite chromosome (*VC1378*) under the control of an arabinose-inducible promoter [39] producing NM565. Saturated overnight cultures of NM565 were grown under repressing conditions ((0.05% D-Fucose(Acros), 0.5% D-Glucose)) in LB and back-diluted to an OD_{600} of 0.001 into repressing conditions or into LB supplemented with indicated concentrations of L-Arabinose. Images were taken starting 2h after back-dilution.

Western Blotting

For *V. cholerae* samples, cultures were lysed in as previously described[40] with slight modification. Cultures were centrifuged and resuspended in Bug Buster protein extraction reagent (EMD Millipore) supplemented with 50μg/mL lysozyme, 25units/mL Benzonase, and 1mM phenylmethylsulfonyl fluoride (PMSF). Samples were then incubated at room temperature for 10min before adding 4xSDS running buffer (250mM Tris-HCl pH 6.8, 40% glycerol, 0.2% bromophenol blue, 20% 2-mercaptoethanol, and 8% SDS) to a concentration of 1x and boiling samples for 30min. *E. coli* samples were lysed by resuspending centrifuged culture directly in 1xSDS running buffer and boiling for 30min. Lysed samples were then run on 4–15% Mini-PROTEAN TGX (BioRad) Stain-Free gels or 4–20% Mini-PROTEAN TGX (BioRad) gels with LiCor Chameleon Duo Pre-Stained Protein Ladder (928–60000). Gels were transferred to Amersham™ Proton™ 0.2μm nitrocellulose membranes soaked in transfer buffer (300mM Tris, 300mM glycine) using a BioRad Trans-Blot SD Semi-Dry Transfer Cell. Membranes were blocked and probed with primary antibodies for 1h each in TBST (20mM Tris, 137mM NaCl, 0.1% TWEEN20 (Sigma-Aldrich)) supplemented with 5% milk. Membranes were washed three times for 10min with TBST and then probed with secondary antibodies in TBST supplemented with 5% milk followed by two additional washes with TBST and one final wash with TBS (20mM Tris, 137mM NaCl). Membranes were allowed to dry before detection. For detection of CrvA-

GFP and CrvB-GFP, Mouse anti-GFP primary antibodies (Roche #11814460001) were used at a 1:2500 dilution. RpoA was used as a loading control and was detected using Mouse anti-RNA polymerase α primary antibodies (BioLegend #663104) at a 1:15,000 dilution. Goat anti-Mouse IRDye 680RD (LiCor #926–68070) was used at a 1:10,000 dilution as a secondary antibody for detection with a LiCor Odyssey CLx-1048 imager operated with Li-Cor Image studio Version 4.0.21. When relevant, membranes were quantified with Li-Cor Image Studio Lite Version 5.2.5.

Phylogenetic analysis

For determining the overall phylogeny of the *Vibrio* genomes, a composite gene comprising the sequences of mreB, gyrB, gapA, ftsZ, pyrH, recA, rpoA, topA, fur, and the 16S RNA sequence, was assembled and used to create a multiple sequence alignment as in[41]. A phylogenetic tree was constructed using BMGE/FastTree[42,43] using the publicly accessible Galaxy@Pasteur server[44]. For determining the phylogeny of Crv proteins, a multiple alignment of the unique sequences of Crv proteins (all found within the Vibrionales clade) and an outgroup of the closest homologs found after excluding the Vibrionales was made using MAFFT [45] with blosum80 [46] as the scoring matrix. Following this multiple alignment, a phylogenetic tree was constructed using BMGE/FastTree [42,43]. To compare the local sequence similarity between the CrvA, CrvB, and CrvY, we divided the sequences into four clades (c = {outgroup, CrvA, CrvB, CrvY}) and calculated a local, windowed alignment score[47] compared to the CrvY clade using the blosum80 scoring matrix.

$$Score(iStrain, \; jReference, \; kPosition) \\ = blosum80(sequence(iStrain, \; kPosition), \; sequence(jReference, \; kPosition)$$

$$WindowedScore(iStrain, \; jReference, \; kPosition) \\ = \frac{\sum_{delta \; = \; -windowSize}^{delta \; = \; +windowSize} Score(iStrain, \; jReference, \; kPosition - delta)}{\mid 2 * window \; size + 1 \mid}$$

$$AveragedWindowedScore \; (kPosition) \\ = \frac{\sum_{strains} \sum_{references} WindowedScore \; (iStrain, \; jReference, \; kPosition)}{nStrains \; nReferences}$$

Osmotic shock

Saturated overnight cultures of *V. cholerae* were diluted into 5mL LB and grown for 6h. Cultures were then spotted onto 1–2% low melting point agarose pads made with M9 as described above, or a hyperosmotic medium (15 mM $(NH_4)_2SO_4$, 100mM KH_2PO_4, 1.7μM $FeSO_4$ EDTA chelate, 0.8% glucose, 0.4% casamino acids, 10mM $MgSO_4$, 10% sucrose). Cells rested on pads for 2min before imaging.

Isolation of Peptidoglycan Sacculi

Sacculi were isolated according to a protocol adapted from[48]. Cultures of *V. cholerae* cells (250mL each) were grown to an OD_{600} of ~1.0. Pellets were harvested at 5,000 ×g

for 10 min at room temperature, resuspend in 3mL of 1x phosphate-buffered saline. Cell suspensions were lysed in 4% boiling SDS stirring at 500rpm for 3h, after which point the heat was turned off and stirring continued overnight. Peptidoglycan (PG) was harvested by ultracentrifugation (400,000xg, 20 minutes, room temperature) and resuspended in ultrapure water followed by three washes in ultrapure water. Washed PG was resuspended in 900μL of 10 mM Tris-HCl (pH 7.2) + 0.06% NaCl and transferred to 2mL tubes previously poked with holes in the tops with a small needle and incubated with 100uL activated Pronase E (100 μg/mL final concentration) at 60 °C for 2 h. Pronase E digestion was stopped by adding 200 μl of 6% SDS to each sample and boiling at 100 °C for 30 min. Pronase E digestion was stopped by adding 200 μl of 6% SDS to each sample and boiling at 100 °C for 30 min. Samples were washed 3 times with ultrapure water in an ultracentrifuge at 400,000 ×g for 20 min at room temperature to remove SDS. Pellets were resuspended in 200ul of "protein polymerization buffer" (50mM HEPES, 150mM NaCl) and stored at 4°C.

Purification of CrvA Protein

The full length of the *crvA* gene was cloned into the pQlinkHC vector by Gibson Assembly. This vector contains a C-terminal poly-Histidine tag and thrombin cleavage site. The plasmid was transformed by electroporation into E. coli BL21 cells (Promega, cat# L1191). Overnight cultures were back-diluted 1:100 into LB containing 100μg/mL carbenicillin and grown at 37 °C shaking. *crvA*-expressing cells were grown to an OD_{600} of ~1.0. At this point the temperature was lowered to 18°C and IPTG was added to a final concentration of 0.2 mM and cells were grown for 15–20h. The cell pellet was harvested by centrifugation at 8,000rpm for 10 minutes at 4°C. The pellet was resuspended in lysis buffer(50 mM Tris pH 7.5, 300mM NaCl, 20mM imidazole, 10% glycerol, cOmplete™ Mini, EDTA-free Protease Inhibitor Cocktail tablets (1 tablet/50ml buffer)) and lysed in an Emulsiflex-05 homogenizer. The lysate was cleared by centrifugation and the supernatant was loaded onto Ni-NTA agarose resin (Qiagen), packed into Econo-Pac® Chromatography Columns (Biorad) pre-calibrated with column buffer (50 mM Tris pH 7.5, 300mM NaCl, 20mM imidazole, 10% glycerol). Lysate and resin were incubated at 4°C with gentle rotation for ~30 minutes. Stoppers were removed and the lysate was allowed to flow through the resin. Resin beds were washed with Column Buffer and eluted with elution buffer (50 mM Tris pH 7.5, 300mM NaCl, 250mM imidazole, 10% glycerol). Fractions were analyzed by SDS-PAGE. Purified protein was flash frozen in liquid nitrogen and stored at −80°C.

in vitro CrvA Peptidoglycan Binding Assay

Purified peptidoglycan was diluted 2x into ice-cold buffer (50mM HEPES, 150mM NaCl) to create +PG buffer. Purified protein (CrvA (0.5 mg/mL), GFP solution (1 mg/ml, lab stock), and WGA (2.5 mg/ml, Thermo Fisher cat# W11261) was thawed on ice and diluted 10x into plan ice-cold buffer as well as into +PG buffer. The samples were then taken off ice and incubated at room temperature for one hour. 20 μL of each was saved for the pre-spin sample. The remaining sample was spun in a tabletop centrifuge at 21,000xg for 20 minutes. The supernatant was removed and 20 μL was saved for the supernatant sample. Pellets were gently washed by slowly pipetting 300 μL of fresh buffer into the tube, spinning again in the tabletop centrifuge, and removing the supernatant. The pellets were resuspended in 300 μL of room temperature buffer and 20 μL was saved for the pellet sample. 2 μL of Lysozyme (5

mg/ml, MP Biomedicals cat# 100834) was added to each of the 20 μL pre-spin, supernatant, and pellet samples and they were incubated at 37°C overnight. Samples were mixed with 2X Laemmli SDS-PAGE loading buffer (Biorad) with 2-mercaptoethanol, loaded onto 4%−20% Mini-PROTEAN TGX precast gels (Biorad), and visualized by Coomassie staining with BioRad Precision Plus Protein Dual Color Standards (161−0374).

Data availability:

The data supporting the findings of the study are available in this article or on the Princeton DataSpace (Link to follow).

Code availability:

The custom MATLAB routines used for processing and analyzing microscopy data are freely available from the corresponding author upon request.

Extended Data

Extended Data Fig. 1. CrvAB sequence alignment and complementation analysis.

Extended Data Fig. 2. Quantification of heterologous CrvAB expression.
A) Curvature of populations expressing an empty vector (+EV) or a plasmid with *crvA*
and *crvB* (+*crvAB*). p-values determined by two-sided Wilcoxon rank sum test; n=300
from three biological replicates. (B(B) Cumulative distribution functions of populations in
A ± bootstrapped 95% confidence intervals. (C) Images represent indicated quantiles from
populations in A.. Each row corresponds to the species labeled to the left of A. Scale bars
are 1μm; images within each species are to scale. (A) The *crvA* and *crvB* open reading
frames drawn to scale at the native locus in *V. cholerae*. (B) Alignment of *V. cholerae*

CrvB amino acid sequence to *V. cholerae* CrvA by Clustalω [49]. (C-E) Curvature of (C) *crvA*, (D) *crvB*, or (E) *crvAB* populations expressing an empty vector (EV) or plasmids with the indicated gene(s). (C-E) Images represent 95th percentile of curvature in respective populations. Scale bars are 1μm; images within each figure panel are to scale. p-values determined by two-sided Wilcoxon rank sum test; n=300 from three biological replicates.
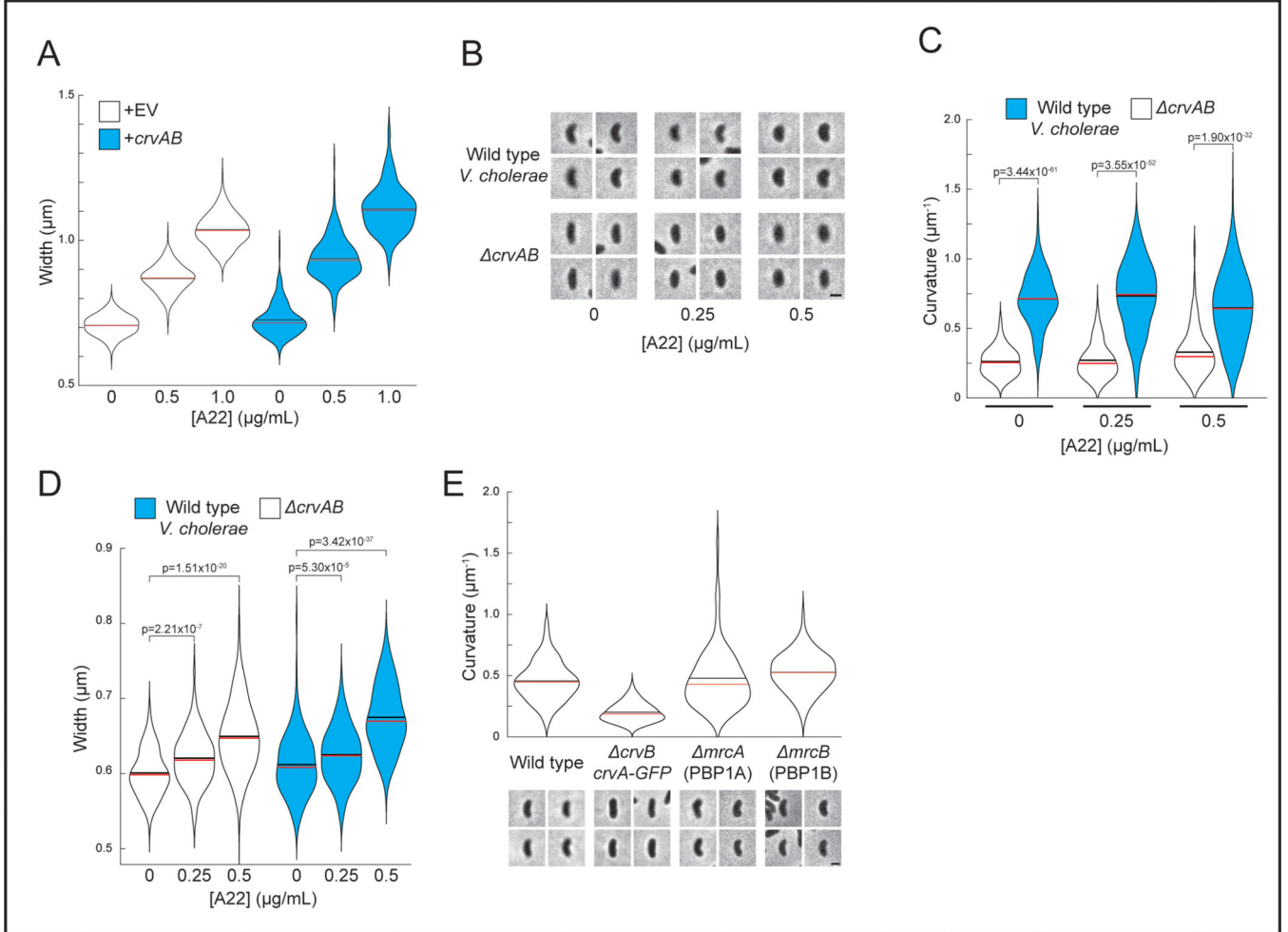
Extended Data Fig. 3. Morphology of *E. coli* and *V. cholerae* after inhibition of PG synthesis machinery.
(A) Quantified cell widths of A22-treated populations of E. coli from Figure 2A. (B) Representative images of wild-type and *crvAB V. cholerae* after growth with the elongasome inhibitor, A22. (C) Quantification of curvature from populations in B. (D) Quantification of cell width from populations in B. (E) Population curvature and representative images of indicated *V. cholerae* strains. n=300 from three biological replicates. (B, E) Images represent 95th percentile of curvature in respective populations. (C,D) p-values from two-sided Wilcoxon rank sum test; n=200 from two biological replicates. Scale bars are 1μm; images within each figure panel are to scale.
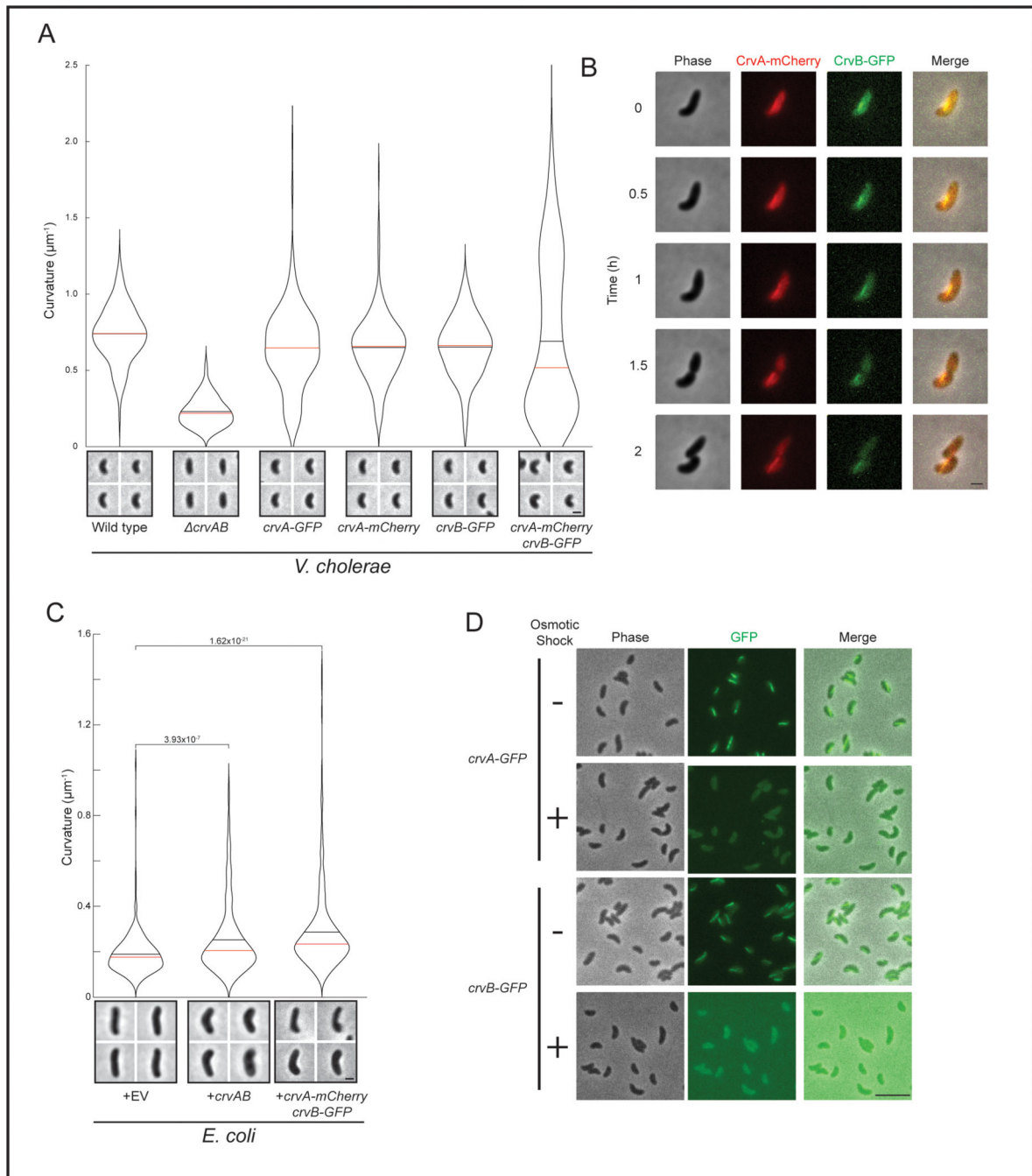
Extended Data Fig. 4. Functionality, time lapse, and osmotic dissociation of fluorescent CrvA and CrvB fusions.

(A) Quantified curvature of populations of *V. cholerae* expressing the indicated fusion proteins from the native genomic locus. Data from wild type and *crvAB* are repeated from Figure 1A. (B) Time lapse images of CrvB-GFP and CrvA-mCherry structures in growing *V. cholerae*. See Movie S1 for full time lapse. (C) Quantified curvature of *E. coli* populations expressing an empty vector (+EV), a plasmid with *crvA* and *crvB* (+crvAB), or the same plasmid with *crvA-mCherry* and *crvB-GFP*. Data from +EV and +crvAB are repeated from Figure 1C. (D) Osmotic shock of *V. cholerae* expressing *crvA-GFP* or *crvB-GFP*. (A,C)

Images were taken 6h after dilution of saturated overnight cultures. Images represent 95th percentile of curvature in respective populations. (C) p-values from two-sided Wilcoxon rank sum test; n=300 from three biological replicates. Scale bars are 1μm in A-C and 5μm in D; images within each figure panel are to scale.
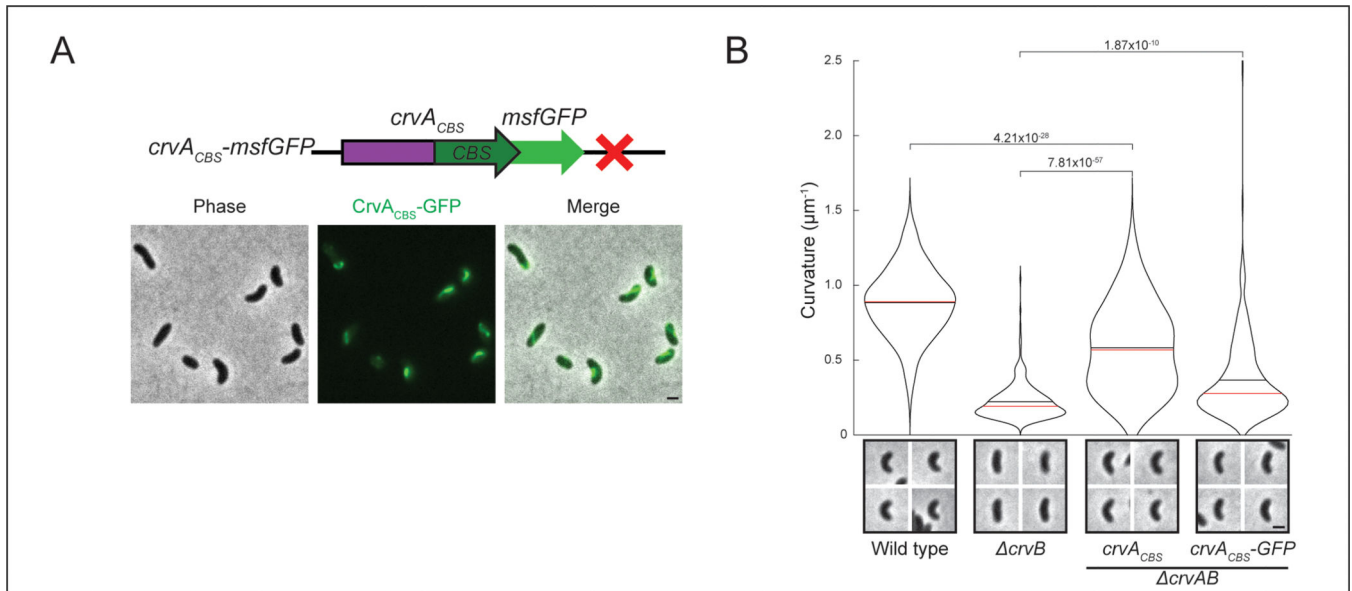
Extended Data Fig. 5. Quantification and localization of $crvA_{CBS}$ in *V. cholerae*.
(A) Schematic of *crv* locus and representative image of cells expressing the $crvA_{CBS}$ chimera tagged with msfGFP (CrvA$_{CBS}$-GFP).((B) Quantified curvature of populations from overnight cultures of indicated *V. cholerae* strains. Data from wild-type, *crvB*, and $crvA_{CBS}$ are repeated from Figure 4. p-values from two-sided Wilcoxon rank sum test; n=300 from three biological replicates.Scale bars are 1μm; images within each figure panel are to scale
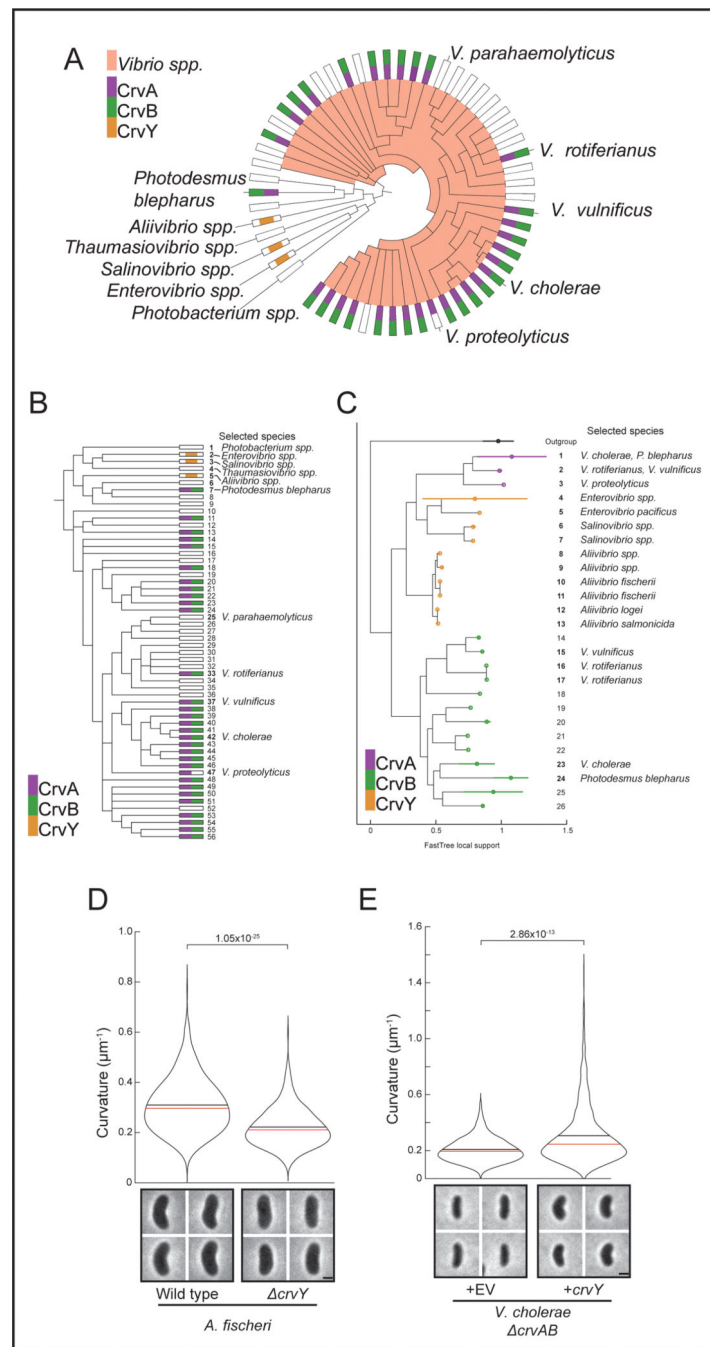
Extended Data Fig. 6. The evolution of CrvA/B/Y and functional study of CrvY.
(A) Extended cladogram from Figure 1B. (B) Linear form of extended cladogram in A. (C) Phylogeny of all sequenced CrvA, CrvB, and CrvY homologs. (D) Curvature of populations of wild-type *A. fischeri* or Δ*crvY*. (E) Curvature of populations of *V. cholera* Δ*crvAB* expressing an empty vector (+EV) or a plasmid with *crvY* from *A. fischeri* (+*crvY*). (A,B) Numbers are "Clade IDs" for reference to Table S2, which contains full composition of terminal nodes. (D) Terminal nodes are placed at the mean ± standard deviation of the sequences collapsed into each node. (D,E) Images represent 95th percentile of curvature in

respective populations. Scale bars are 1µm; images within each figure panel are to scale. p-values determined by two-sided Wilcoxon rank sum test; n=300 from three biological replicates.
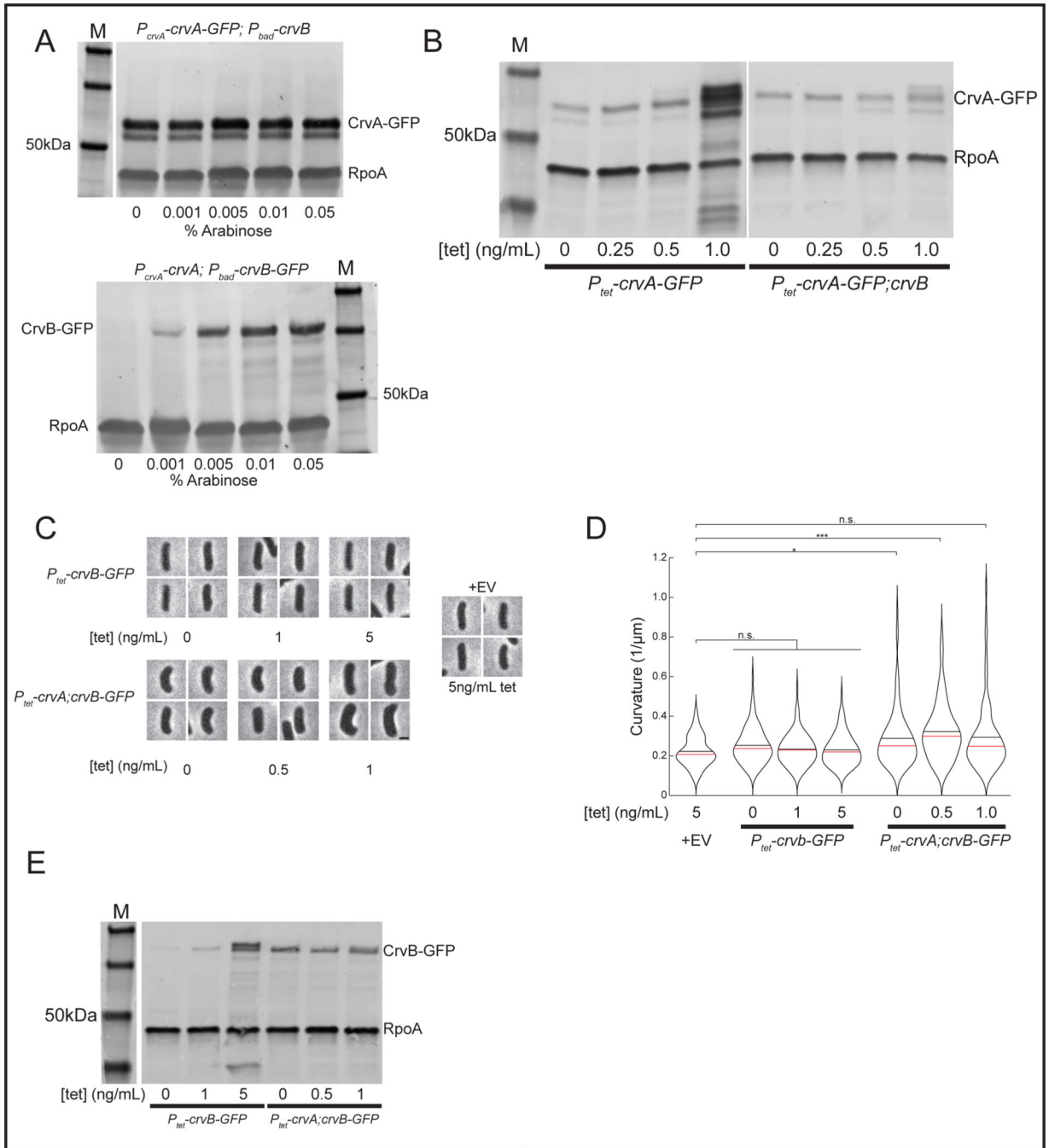
Extended Data Figure 7. Comparison of CrvA and CrvB concentrations under inducible expression.
(A) Western blots of CrvA-GFP (top) and CrvB-GFP (bottom) quantified in Figure 5E with molecular weight standards (M). Separate molecular weight standard in top panel is from the same blot as samples to right. Representative of three biological replicates

with similar results. (B) Western blots of *crvA-GFP* and *crvA-GFP*,*crvB* overexpression from Figure 6A-B with molecular weight standard (M). Separate left and right panels are from the same blot. Representative of two biological replicates with similar results. (C) Representative images from anydrotetracycline (tet) overexpression of CrvA and CrvB-GFP in E. coli. Scale bar is 1μm; all images are to scale. (D) Quantification of curvature from populations in C. n.s.=confidence <95%; *=confidence >95%; **=confidence >99%; ***=confidence >99.9% (see Table S3 for exact p-values); two-sided Wilcoxon rank sum test with Bonferroni correction; n=100 from two biological replicates. (E) Western blot of crvB-GFP and crvA;crvB-GFP overexpression from (C). Separate molecular weight standard (M) and right panel are from the same blot. Representative of two biological replicates with similar results.
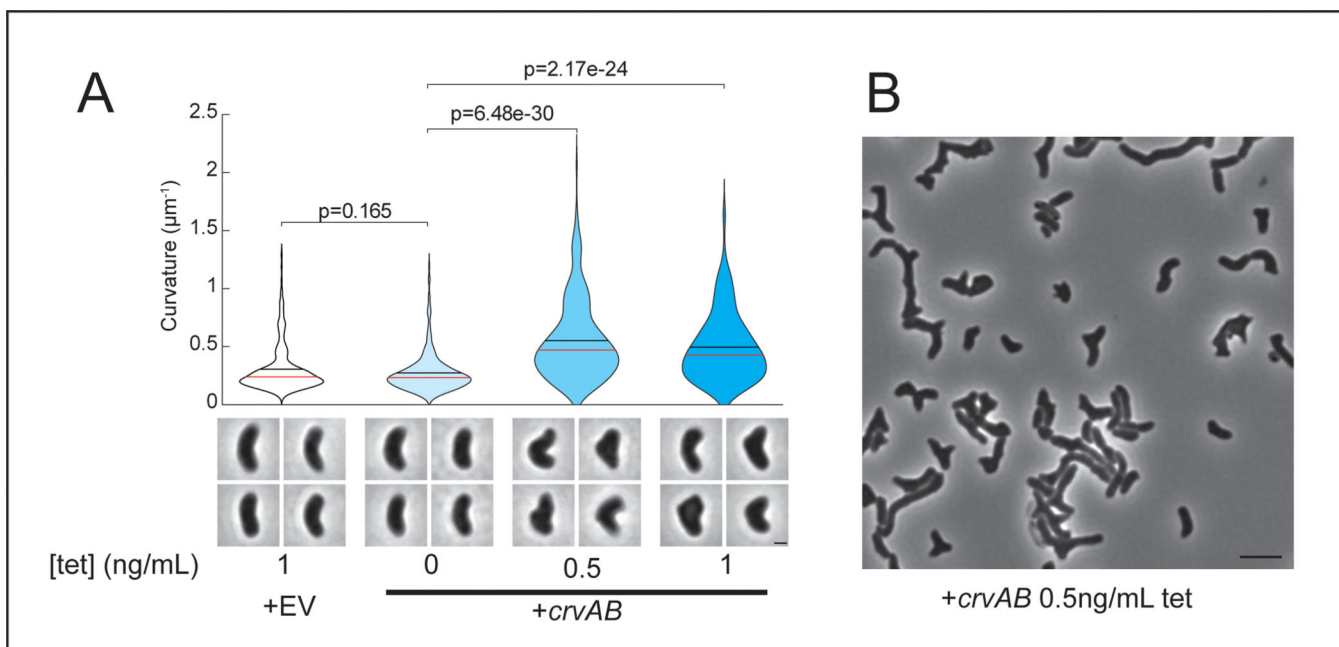
Extended Data Fig. 8. CrvAB overexpression drives early curvature.
(A) Curvature and representative images of populations overexpressing CrvA and CrvB two hours after back-dilution into media containing anhydrotetracycline. (B) Phase contrast image from A showing the extreme range of curvatures upon overexpression that are not captured by our quantitative analysis. (A) p-values calculated from two-sided Wilcoxon rank sum test; n=300 from three biological replicates. Scale bars are 1μm in A and 5μm in B; images within each figure panel are to scale.

Supplementary Material

Refer to Web version on PubMed Central for supplementary material.

Acknowledgments:

References:

1. Young KD The selective value of bacterial shape. Microbiol Mol Biol Rev 70, 660–703, doi:10.1128/MMBR.00001-06 (2006). [PubMed: 16959965]

2. Yang DC, Blair KM & Salama NR Staying in Shape: the Impact of Cell Shape on Bacterial Survival in Diverse Environments. Microbiol Mol Biol Rev 80, 187–203, doi:10.1128/MMBR.00031-15 (2016). [PubMed: 26864431]

3. Orr RG, Cheng X, Vidali L. & Bezanilla M. Orchestrating cell morphology from the inside out - using polarized cell expansion in plants as a model. Curr Opin Cell Biol 62, 46–53, doi:10.1016/j.ceb.2019.08.004 (2019). [PubMed: 31546159]

4. Vogel V. & Sheetz M. Local force and geometry sensing regulate cell functions. Nat Rev Mol Cell Biol 7, 265–275, doi:10.1038/nrm1890 (2006). [PubMed: 16607289]

5. Caccamo PD & Brun YV The Molecular Basis of Noncanonical Bacterial Morphology. Trends Microbiol, doi:10.1016/j.tim.2017.09.012 (2017).

6. Taylor JA, Sichel SR & Salama NR Bent Bacteria: A Comparison of Cell Shape Mechanisms in Proteobacteria. Annu Rev Microbiol 73, 457–480, doi:10.1146/annurev-micro-020518-115919 (2019). [PubMed: 31206344]

7. Typas A, Banzhaf M, Gross CA & Vollmer W. From the regulation of peptidoglycan synthesis to bacterial growth and morphology. Nat Rev Microbiol 10, 123–136, doi:10.1038/nrmicro2677 (2011). [PubMed: 22203377]

8. Yang X. et al. GTPase activity-coupled treadmilling of the bacterial tubulin FtsZ organizes septal cell wall synthesis. Science 355, 744–747, doi:10.1126/science.aak9995 (2017). [PubMed: 28209899]

9. Bisson-Filho AW et al. Treadmilling by FtsZ filaments drives peptidoglycan synthesis and bacterial cell division. Science 355, 739–743, doi:10.1126/science.aak9973 (2017). [PubMed: 28209898]

10. Ursell TS et al. Rod-like bacterial shape is maintained by feedback between cell curvature and cytoskeletal localization. Proc Natl Acad Sci U S A 111, E1025–1034, doi:10.1073/pnas.1317174111 (2014). [PubMed: 24550515]

11. Garner EC et al. Coupled, circumferential motions of the cell wall synthesis machinery and MreB filaments in B. subtilis. Science 333, 222–225, doi:10.1126/science.1203285 (2011). [PubMed: 21636745]

12. Schuech R, Hoehfurtner T, Smith DJ & Humphries S. Motile curved bacteria are Pareto-optimal. Proc Natl Acad Sci U S A 116, 14440–14447, doi:10.1073/pnas.1818997116 (2019). [PubMed: 31266896]

13. Bartlett TM et al. A Periplasmic Polymer Curves Vibrio cholerae and Promotes Pathogenesis. Cell 168, 172–185 e115, doi:10.1016/j.cell.2016.12.019 (2017). [PubMed: 28086090]

14. Persat A, Stone HA & Gitai Z. The curved shape of Caulobacter crescentus enhances surface colonization in flow. Nat Commun 5, 3824, doi:10.1038/ncomms4824 (2014). [PubMed: 24806788]

15. Ausmees N, Kuhn JR & Jacobs-Wagner C. The bacterial cytoskeleton: an intermediate filament-like function in cell shape. Cell 115, 705–713, doi:10.1016/s0092-8674(03)00935-8 (2003). [PubMed: 14675535]

16. Charbon G, Cabeen MT & Jacobs-Wagner C. Bacterial intermediate filaments: in vivo assembly, organization, and dynamics of crescentin. Genes Dev 23, 1131–1144, doi:10.1101/gad.1795509 (2009). [PubMed: 19417107]

17. Cabeen MT et al. Bacterial cell curvature through mechanical control of cell growth. EMBO J 28, 1208–1219, doi:10.1038/emboj.2009.61 (2009). [PubMed: 19279668]

18. Billini M, Biboy J, Kuhn J, Vollmer W. & Thanbichler M. A specialized MreB-dependent cell wall biosynthetic complex mediates the formation of stalk-specific peptidoglycan in Caulobacter

crescentus. PLoS Genet 15, e1007897, doi:10.1371/journal.pgen.1007897 (2019). [PubMed: 30707707]

19. Wagner JK, Galvani CD & Brun YV Caulobacter crescentus requires RodA and MreB for stalk synthesis and prevention of ectopic pole formation. J Bacteriol 187, 544–553, doi:10.1128/JB.187.2.544-553.2005 (2005). [PubMed: 15629926]

20. Dent EW, Gupton SL & Gertler FB The growth cone cytoskeleton in axon outgrowth and guidance. Cold Spring Harb Perspect Biol 3, doi:10.1101/cshperspect.a001800 (2011).

21. Brown JW & McKnight CJ Molecular model of the microvillar cytoskeleton and organization of the brush border. PLoS One 5, e9406, doi:10.1371/journal.pone.0009406 (2010). [PubMed: 20195380]

22. Farmer Iii JJ, Michael Janda J, Brenner FW, Cameron DN & Birkhead KM Vibrio. Bergey's Manual of Systematics of Archaea and Bacteria, 1–79 (2015).

23. Cowles KN & Gitai Z. Surface association and the MreB cytoskeleton regulate pilus production, localization and function in Pseudomonas aeruginosa. Mol Microbiol 76, 1411–1426, doi:10.1111/j.1365-2958.2010.07132.x (2010). [PubMed: 20398206]

24. Srivastava P, Demarre G, Karpova TS, McNally J. & Chattoraj DK Changes in nucleoid morphology and origin localization upon inhibition or alteration of the actin homolog, MreB, of Vibrio cholerae. J Bacteriol 189, 7450–7463, doi:10.1128/JB.00362-07 (2007). [PubMed: 17704222]

25. Cameron TA, Anderson-Furgeson J, Zupan JR, Zik JJ & Zambryski PC Peptidoglycan synthesis machinery in Agrobacterium tumefaciens during unipolar growth and cell division. Mbio 5, e01219–01214, doi:10.1128/mBio.01219-14 (2014). [PubMed: 24865559]

26. Howell M. et al. Agrobacterium tumefaciens divisome proteins regulate the transition from polar growth to cell division. Mol Microbiol 111, 1074–1092, doi:10.1111/mmi.14212 (2019). [PubMed: 30693575]

27. Ouzounov N. et al. MreB Orientation Correlates with Cell Diameter in Escherichia coli. Biophys J 111, 1035–1043, doi:10.1016/j.bpj.2016.07.017 (2016). [PubMed: 27602731]

28. Dorr T. et al. Differential requirement for PBP1a and PBP1b in in vivo and in vitro fitness of Vibrio cholerae. Infect Immun 82, 2115–2124, doi:10.1128/IAI.00012-14 (2014). [PubMed: 24614657]

29. Bratton BP, Shaevitz JW, Gitai Z. & Morgenstein RM MreB polymers and curvature localization are enhanced by RodZ and predict E. coli's cylindrical uniformity. Nat Commun 9, 2797, doi:10.1038/s41467-018-05186-5 (2018). [PubMed: 30022070]

30. Hussain S. et al. MreB filaments align along greatest principal membrane curvature to orient cell wall synthesis. Elife 7, doi:10.7554/eLife.32471 (2018).

31. Schierle CF et al. The DsbA signal sequence directs efficient, cotranslational export of passenger proteins to the Escherichia coli periplasm via the signal recognition particle pathway. J Bacteriol 185, 5706–5713, doi:10.1128/jb.185.19.5706-5713.2003 (2003). [PubMed: 13129941]

32. Weaver AI et al. Genetic Determinants of Penicillin Tolerance in Vibrio cholerae. Antimicrob Agents Chemother 62, doi:10.1128/AAC.01326-18 (2018).

33. Taguchi A, Kahne D. & Walker S. Chemical tools to characterize peptidoglycan synthases. Curr Opin Chem Biol 53, 44–50, doi:10.1016/j.cbpa.2019.07.009 (2019). [PubMed: 31466035]

34. Battistuzzi FU, Feijao A. & Hedges SB A genomic timescale of prokaryote evolution: insights into the origin of methanogenesis, phototrophy, and the colonization of land. BMC Evol Biol 4, 44, doi:10.1186/1471-2148-4-44 (2004). [PubMed: 15535883]

35. Jiang C, Brown PJ, Ducret A. & Brun YV Sequential evolution of bacterial morphology by co-option of a developmental regulator. Nature 506, 489–493, doi:10.1038/nature12900 (2014). [PubMed: 24463524]

36. Skorupski K. & Taylor RK Positive selection vectors for allelic exchange. Gene 169, 47–52 (1996). [PubMed: 8635748]

37. Edwards RA, Keller LH & Schifferli DM Improved allelic exchange vectors and their use to analyze 987P fimbria gene expression. Gene 207, 149–157, doi:10.1016/s0378-1119(97)00619-7 (1998). [PubMed: 9511756]

38. Bina XR, Wong EA, Bina TF & Bina JE Construction of a tetracycline inducible expression vector and characterization of its use in Vibrio cholerae. Plasmid 76, 87–94, doi:10.1016/j.plasmid.2014.10.004 (2014). [PubMed: 25451701]

39. Guzman LM, Belin D, Carson MJ & Beckwith J. Tight regulation, modulation, and high-level expression by vectors containing the arabinose PBAD promoter. J Bacteriol 177, 4121–4130 (1995). [PubMed: 7608087]

40. Bridges AA & Bassler BL The intragenus and interspecies quorum-sensing autoinducers exert distinct control over Vibrio cholerae biofilm formation and dispersal. PLoS Biol 17, e3000429, doi:10.1371/journal.pbio.3000429 (2019). [PubMed: 31710602]

41. Sawabe T. et al. Updating the Vibrio clades defined by multilocus sequence phylogeny: proposal of eight new clades, and the description of Vibrio tritonius sp. nov. Front Microbiol 4, 414, doi:10.3389/fmicb.2013.00414 (2013). [PubMed: 24409173]

42. Criscuolo A. & Gribaldo S. BMGE (Block Mapping and Gathering with Entropy): a new software for selection of phylogenetic informative regions from multiple sequence alignments. BMC Evol Biol 10, 210, doi:10.1186/1471-2148-10-210 (2010). [PubMed: 20626897]

43. Guindon S. et al. New algorithms and methods to estimate maximum-likelihood phylogenies: assessing the performance of PhyML 3.0. Syst Biol 59, 307–321, doi:10.1093/sysbio/syq010 (2010). [PubMed: 20525638]

44. Afgan E. et al. The Galaxy platform for accessible, reproducible and collaborative biomedical analyses: 2018 update. Nucleic Acids Res 46, W537–W544, doi:10.1093/nar/gky379 (2018). [PubMed: 29790989]

45. Katoh K. & Standley DM MAFFT multiple sequence alignment software version 7: improvements in performance and usability. Mol Biol Evol 30, 772–780, doi:10.1093/molbev/mst010 (2013). [PubMed: 23329690]

46. Henikoff S. & Henikoff JG Amino acid substitution matrices from protein blocks. Proc Natl Acad Sci U S A 89, 10915–10919, doi:10.1073/pnas.89.22.10915 (1992). [PubMed: 1438297]

47. Capra JA & Singh M. Predicting functionally important residues from sequence conservation. Bioinformatics 23, 1875–1882, doi:10.1093/bioinformatics/btm270 (2007). [PubMed: 17519246]

48. Desmarais SM, Cava F, de Pedro MA & Huang KC Isolation and preparation of bacterial cell walls for compositional analysis by ultra performance liquid chromatography. J Vis Exp, e51183, doi:10.3791/51183 (2014). [PubMed: 24457605]

49. Sievers F. et al. Fast, scalable generation of high-quality protein multiple sequence alignments using Clustal Omega. Mol Syst Biol 7, 539, doi:10.1038/msb.2011.75 (2011). [PubMed: 21988835]

50. Thelin KH & Taylor RK Toxin-coregulated pilus, but not mannose-sensitive hemagglutinin, is required for colonization by Vibrio cholerae O1 El Tor biotype and O139 strains. Infect Immun 64, 2853–2856 (1996). [PubMed: 8698524]

51. Simon R, Quandt J. & Klipp W. New derivatives of transposon Tn5 suitable for mobilization of replicons, generation of operon fusions and induction of genes in gram-negative bacteria. Gene 80, 161–169, doi:10.1016/0378-1119(89)90262-x (1989). [PubMed: 2551782]

52. Blattner FR et al. The complete genome sequence of Escherichia coli K-12. Science 277, 1453–1462, doi:10.1126/science.277.5331.1453 (1997). [PubMed: 9278503]

53. Rahme LG et al. Common virulence factors for bacterial pathogenicity in plants and animals. Science 268, 1899–1902, doi:10.1126/science.7604262 (1995). [PubMed: 7604262]

54. Evinger M. & Agabian N. Envelope-associated nucleoid from Caulobacter crescentus stalked and swarmer cells. J Bacteriol 132, 294–301 (1977). [PubMed: 334726]

55. Gitai Z, Dye N. & Shapiro L. An actin-like gene can determine cell polarity in bacteria. Proc Natl Acad Sci U S A 101, 8643–8648, doi:10.1073/pnas.0402638101 (2004). [PubMed: 15159537]

56. Watson B, Currier TC, Gordon MP, Chilton MD & Nester EW Plasmid required for virulence of Agrobacterium tumefaciens. J Bacteriol 123, 255–264 (1975). [PubMed: 1141196]

57. Boettcher KJ & Ruby EG Depressed light emission by symbiotic Vibrio fischeri of the sepiolid squid Euprymna scolopes. J Bacteriol 172, 3701–3706, doi:10.1128/jb.172.7.3701-3706.1990 (1990). [PubMed: 2163384]

58. Dunn AK, Millikan DS, Adin DM, Bose JL & Stabb EV New rfp- and pES213-derived tools for analyzing symbiotic Vibrio fischeri reveal patterns of infection and lux expression in situ. Appl Environ Microbiol 72, 802–810, doi:10.1128/AEM.72.1.802-810.2006 (2006). [PubMed: 16391121]

59. Schweizer HP Escherichia-Pseudomonas shuttle vectors derived from pUC18/19. Gene 97, 109–121, doi:10.1016/0378-1119(91)90016-5 (1991). [PubMed: 1899844]

60. Thanbichler M, Iniesta AA & Shapiro L. A comprehensive set of plasmids for vanillate- and xylose-inducible gene expression in Caulobacter crescentus. Nucleic Acids Res 35, e137, doi:10.1093/nar/gkm818 (2007). [PubMed: 17959646]
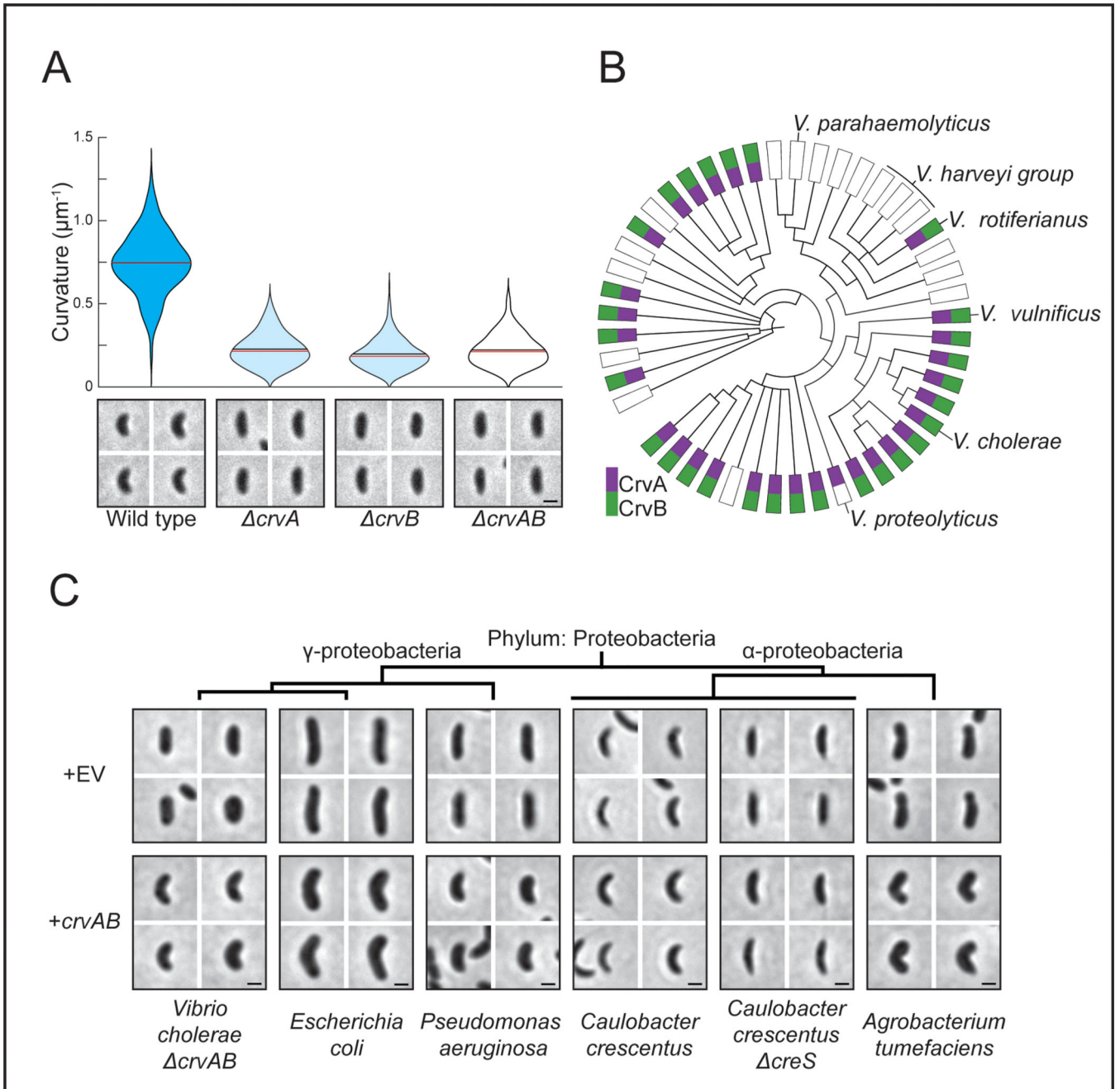
Figure 1. CrvA and CrvB curve bacterial cells.

(A) Quantified curvature of populations from indicated *V. cholerae* strains. Horizontal bars represent mean (black) and median (red). (B) Presence of CrvA and CrvB homologs across *Vibrio* species. Clade structure drawn according to framework outlined in [41]. (C) Heterologous expression of *crvA* and *crvB* (+*crvAB*) or empty vector (+EV). Brackets indicate phylogenetic relationships between species Median curvature of +*crvAB* is significantly higher than +EV in each species (p ≤ 3.74×10⁻⁵); two-sided Wilcoxon rank sum test, n=300 from three biological replicates (see Extended Data Figure 2 for quantified populations). (A,C) Single-cell curvature measured using Morphometrics [10].

Images represent 95th percentile of curvature in respective populations. Scale bars are 1μm and images within each figure panel are to scale.
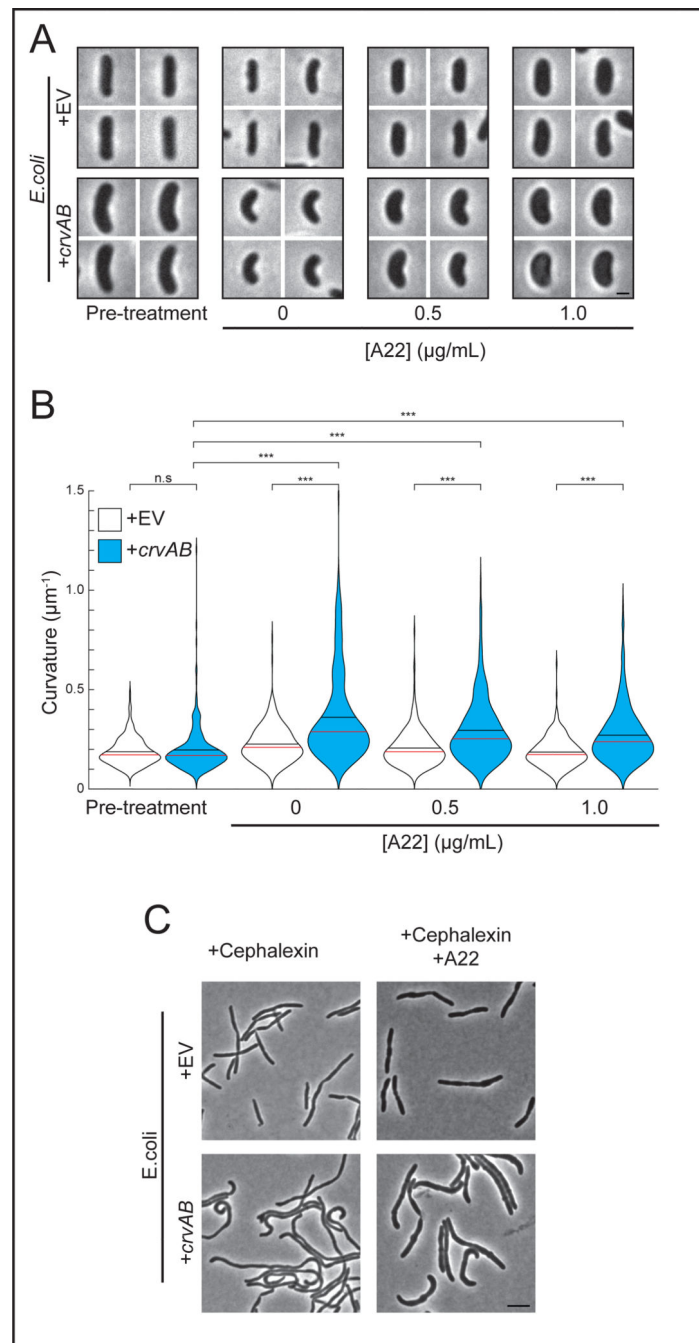
Figure 2. CrvA and CrvB curve *E. coli* despite inhibition of core machinery.

(A) *E. coli* expressing *crvA* and *crvB* (+*crvAB*) or empty vector (+EV) before (Pre-treatment) and after treatment with the elongasome inhibitor, A22. Scale bar is 1μm and all images are to scale.

(B) Quantified cell curvatures of A22-treated populations in A. Two-sided Wilcoxon rank sum test with Bonferroni correction; n=300 from three biological replicates. n.s.= confidence <95%; *= confidence >95%; **= confidence >99%; ***= confidence >99.9% (see Supplementary Table 3 for exact p-values). (C) *E. coli* after treatment with A22 and

the divisome inhibitor, cephalexin. Scale bar is 5μm; all images are to scale. Representative of two biological replicates with similar results. (A) Images represent 95th percentile of curvature in respective populations.
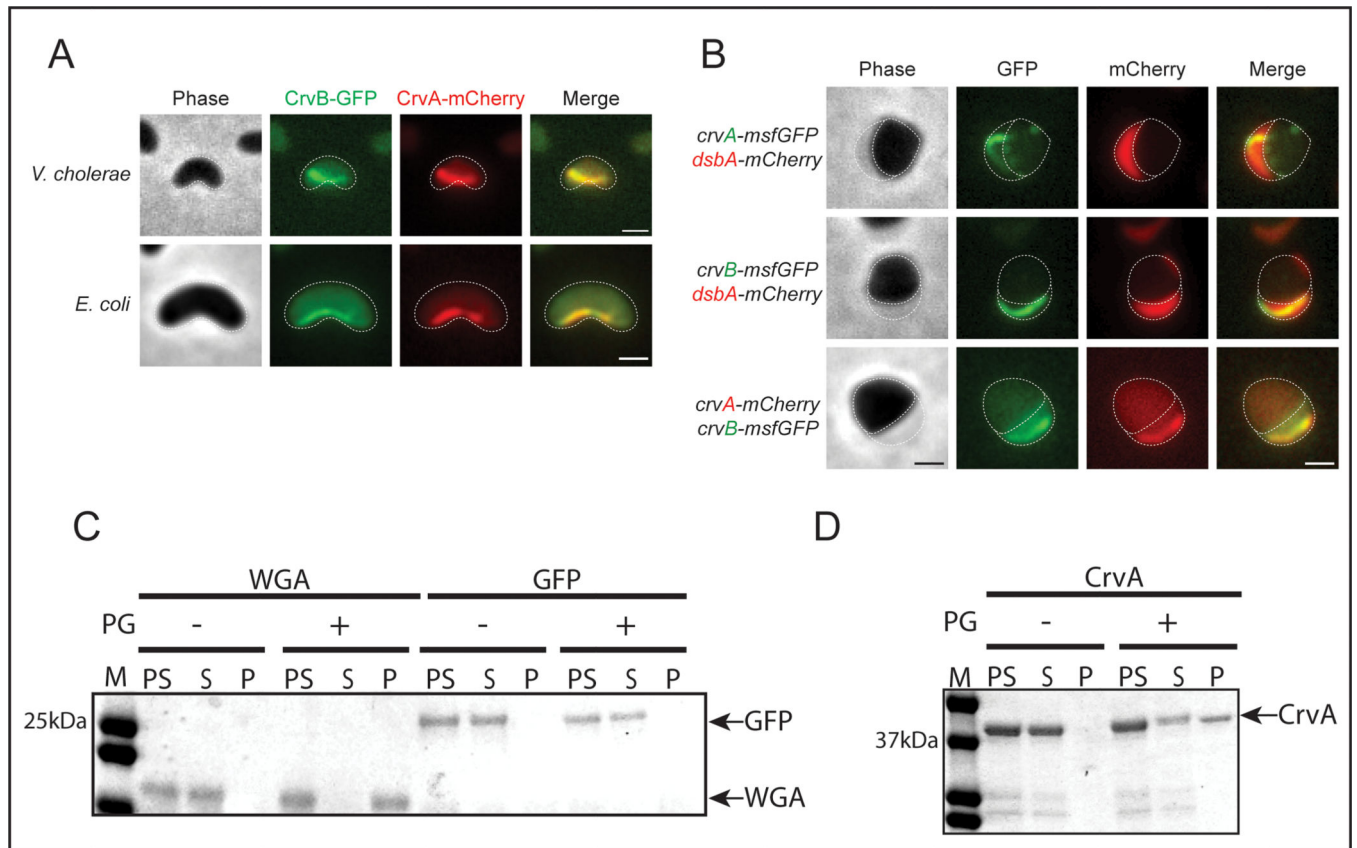
Figure 3. CrvA and CrvB break symmetry by forming a periplasmic filament that binds PG.
(A) Curved *V. cholerae* and *E. coli* cells expressing CrvB-GFP and CrvA-mCherry fusions.
(B) Fluorescent CrvA and CrvB filaments with periplasmic DsbA-mCherry in *V. cholerae*
after moenomycin treatment. (C,D) SDS-PAGE of PG containing (+) or PG lacking (−)
pre-spin (PS), supernatant (S), and pellet (P) fractions from co-sedimentation assay with
molecular weight standard (M) Representative of three independent experiments with
similar results. (A,B) Dotted lines represent outline of cell body and periplasm. Scale bars
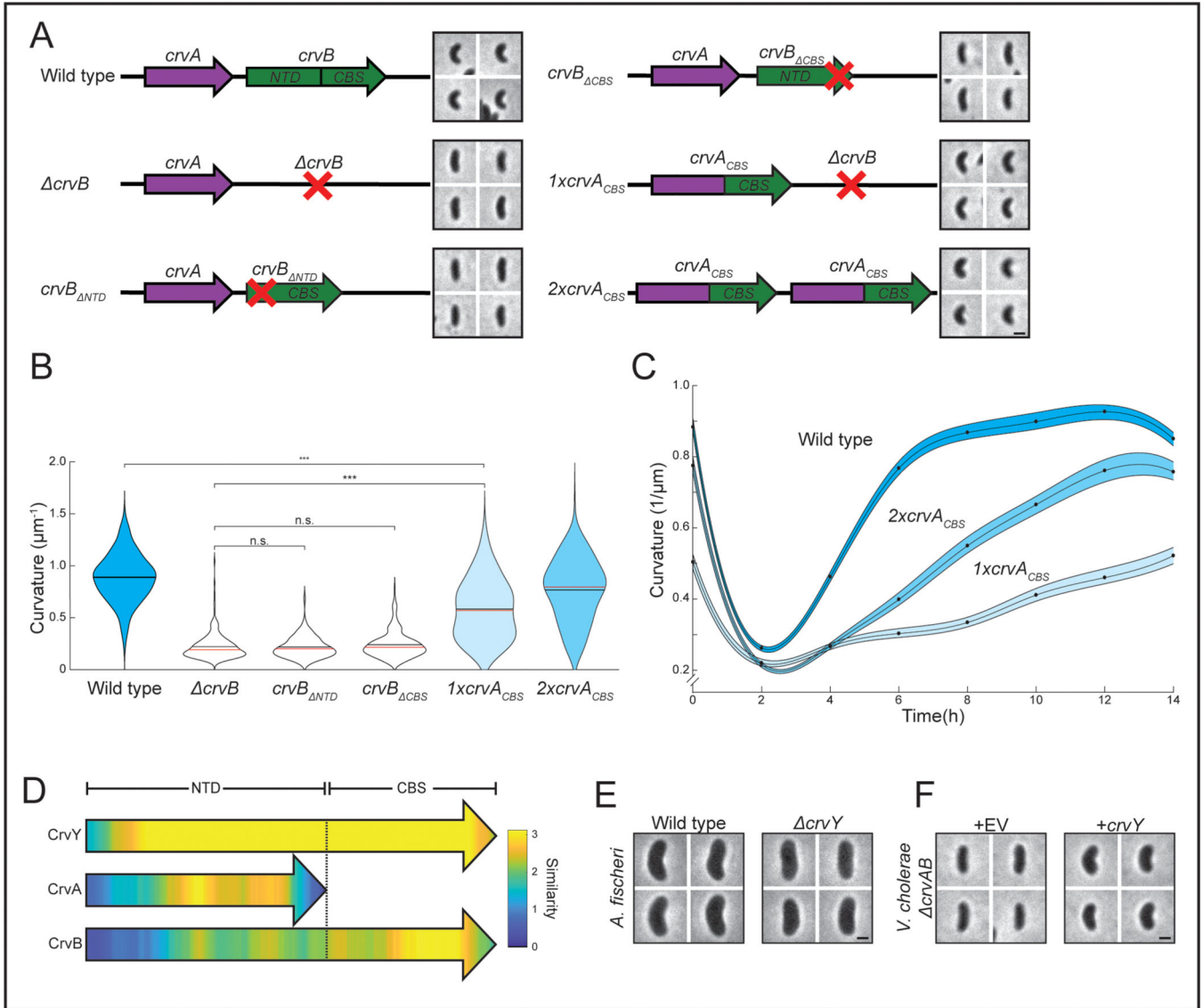are 1μm; images within each figure panel are to scale.

Figure 4. CrvA and CrvB induce curvature more rapidly than the sum of their parts.
(A) Schematic of the *crvAB* locus in *crvB* truncation mutants and *crvA_{CBS}* chimeras with representative images from saturated overnight cultures. (B) Quantified cell curvatures from populations of indicated strains from A. (C) Dynamics of mean cell curvature (±bootstrapped 95% confidence intervals) after 1000-fold dilution from saturated overnight cultures of wild type (WT) and strains expressing one (*1xcrvA_{CBS}*) or two (*2xcrvA_{CBS}*) copies of *crvA_{CBS}*. For each point, n=431–647 from three biological replicates. (D) Pairwise sequence alignment of all sequenced CrvA, CrvB, and CrvY homologs to CrvY. Sequence alignment and local similarity using the BLOSUM80 scoring matrix. (E) Morphology of *A. fischeri* Δ*crvY* mutant. (F) Morphology of *V. cholerae* Δ*crvAB* expressing *crvY*. (A,B) *crvA_{CBS}* overnight culture is the 0h time point from C (B) n.s.=confidence <95%; *=confidence >95%; **=confidence >99%; ***=confidence >99.9% (see Supplementary Table 3 for exact p-values); two-sided Wilcoxon rank sum test with Bonferroni correction; n=300 from three biological replicates. (A,E,F) Images represent 95th percentile of

curvature in respective populations. Scale bars are 1μm; images within each figure panel are to scale. (E,F) See Extended Data Figure 3 for population measurements.
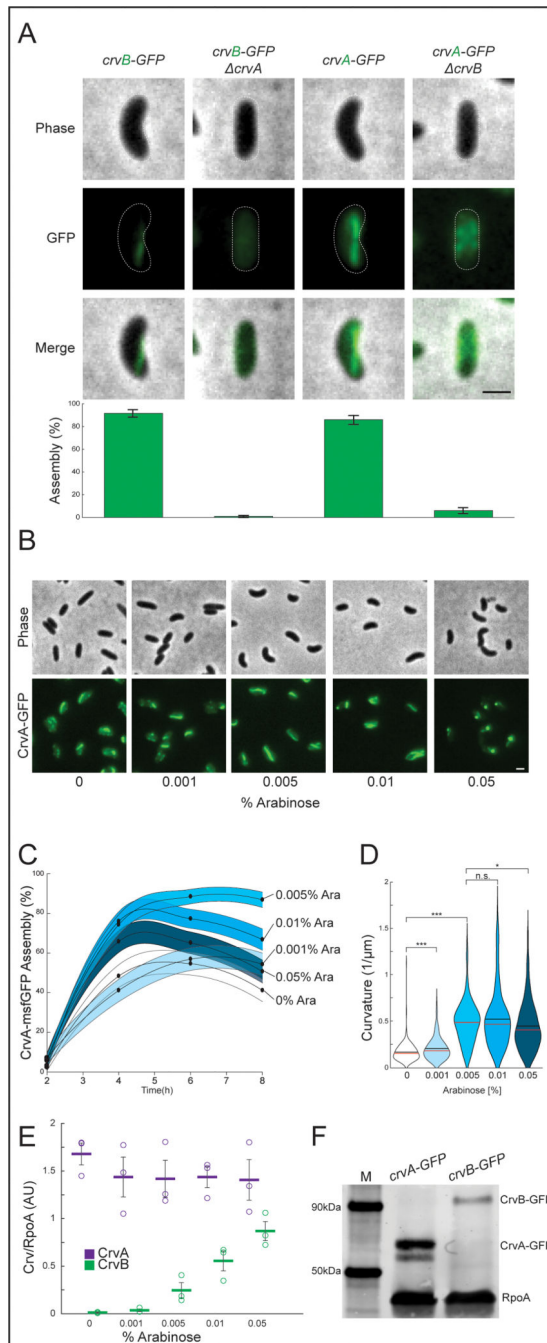
Figure. 5. CrvA and CrvB synergize to promote filament assembly in *V. cholerae*
(A) CrvA-GFP and CrvB-GFP filament assembly in deletion mutants. (top) Representative cells (bottom) Quantification of assembly. Agresti-Coull estimate of percent of population with fluorescent filament similar to those in the wild-type background ($\tilde{p}$) and its 95% confidence interval. n=300 from three biological replicates. Samples taken from cultures 6h after dilution from saturated overnight cultures. (B) Representative fields after induction of *Pbad-crvB*. (C) Dynamics of Agresti-Coull estimate of percent of population with assembled CrvA-GFP structures ($\tilde{p}$) and its 95% confidence interval. n=300 from three

biological replicates. (D) End point curvature measurements from B. n.s.=confidence <95%; *=confidence >95%; **=confidence >99%; ***=confidence >99.9% (see Supplementary Table 3 for exact p-values); two-sided Wilcoxon rank sum test with Bonferroni correction; n=300 from three biological replicates. (E) CrvA-GFP or CrvB-GFP levels during induction of *Pbad* in B-D quantified by western blot. Mean signal in arbitrary units normalized to RpoA loading control ± SEM; n=3 from three biological replicates. (F) Western blot of CrvA-GFP and CrvB-GFP under native regulation and molecular weight standard (M). Representative of three biological replicates with similar results. (E) Horizontal lines represent mean ± standard error of three biological replicates. (A-B) Scale bars are 1μm; images within each figure panel are to scale.
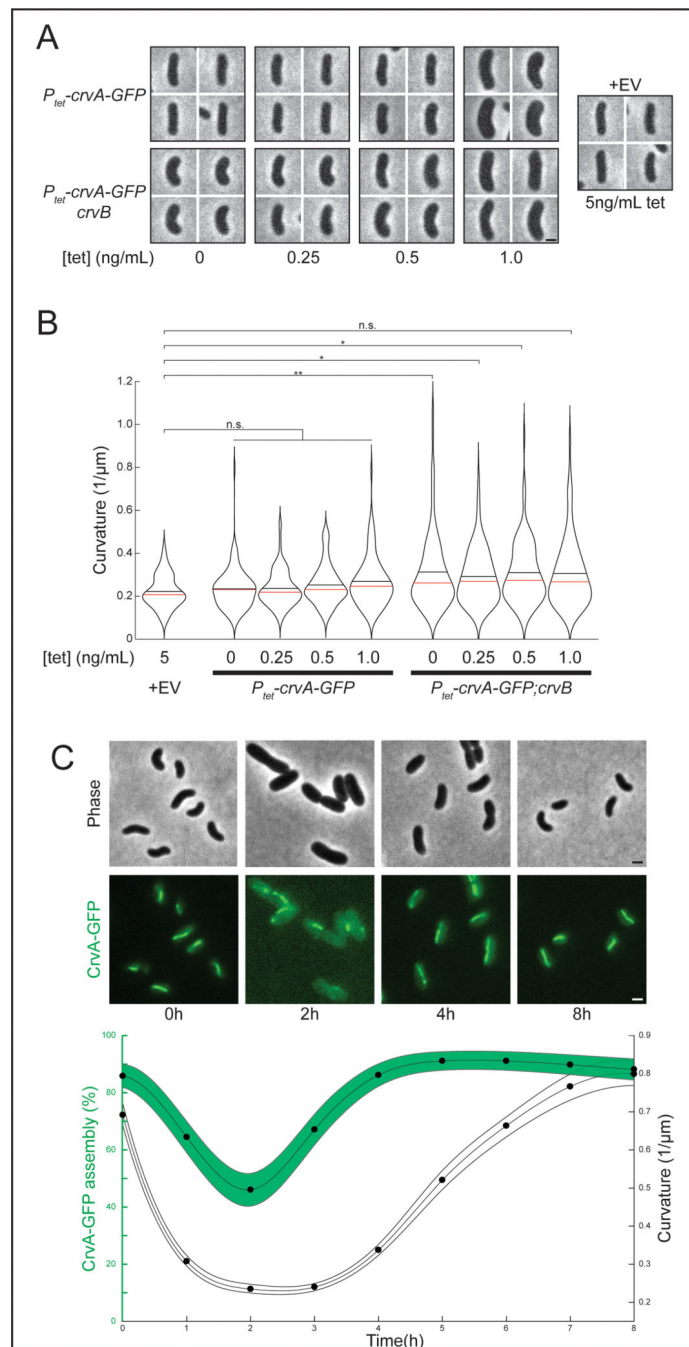
Figure 6. CrvB is required for CrvA activity in *E. coli* and CrvA localization drives shape dynamics in *V. cholerae*.

Representative images from anhydrotetracycline (tet) overexpression of CrvAB in *E. coli*. (B) Quantification of populations from A. n.s.=confidence <95%; *=confidence >95%; **=confidence >99%; ***=confidence >99.9% (see Supplementary Table 3 for exact p-values); two-sided Wilcoxon rank sum test with Bonferroni correction; n=100 from two biological replicates (C) Dynamics of *V. cholerae* mean curvature (±bootstrapped 95% confidence intervals) and CrvA-GFP filament assembly after dilution from saturated overnight cultures ± 95% confidence intervals. Assembly is the Agresti-Coull estimate of

percent of population with assembled structures ($\tilde{p}$) and its 95% confidence interval. n=300 for each point from three biological replicates. (A) Images represent 95th percentile of curvature in respective populations. (A,C) Scale bars are 1μm; images within each figure panel are to scale.